CWP-787
February 2014



Understanding the reverse time migration backscattering: Noise or signal?

Esteban Díaz Pantin

- Master of Science Thesis - Geophysics

Defended on January 31, 2014

Advisor:	Prof. Paul Sava
Committee Members:	Prof. Yaoguo Li
	Prof. Luis Tenorio

Center for Wave Phenomena
Colorado School of Mines
Golden, Colorado 80401
303.384.2178
http://cwp.mines.edu

UNDERSTANDING THE REVERSE TIME MIGRATION BACKSCATTERING: NOISE OR SIGNAL?

by

Esteban Fernando Díaz Pantin

ABSTRACT

Reverse time migration (RTM) backscattered events are produced by the cross-correlation between waves reflected from sharp interfaces (e.g. the top of salt bodies). Commonly, these events are seen as a drawback for the RTM method because they obstruct the image of the geologic structure. Many strategies have been developed to filter out the artifacts from the conventional image. However, these events contain information that can be used to analyze kinematic synchronization between source and receiver wavefields reconstructed in the subsurface. Numeric and theoretical analysis indicate the sensitivity of the backscattered energy to velocity accuracy: an accurate velocity model maximizes the backscattered artifacts. The analysis of RTM extended images can be used as a quality control tool and as input to velocity analysis designed to constrain salt models and sediment velocity.

The analysis in this thesis suggest that we can use backscattering events along with reflection data to define a joint optimization problem for velocity model building. The gradient required for model optimization suffers from cross-talk, similar to the more conventional RTM images. In order to avoid the cross-talk, I use a directional filter based on Poynting vectors which preserves the components of the wavefield traveling in the same direction. Using backscattered waves for constraining the velocity in the sediment section requires defining the top of salt in advance, which implies a dynamic workflow for model building in salt environments where both sediment velocity and salt interface change iteratively during inversion.

TABLE OF CONTENTS

ABSTRACT iii

LIST OF FIGURES vi

LIST OF ABBREVIATIONS ix

ACKNOWLEDGMENTS x

DEDICATION xi

CHAPTER 1 INTRODUCTION 1

CHAPTER 2 KINEMATIC AND FOCUSING PROPERTIES OF RTM BACKSCATTERING[1] 3

2.1 Introduction 3

2.2 Conventional imaging condition 6

2.2.1 Backscattered events in the conventional image 8

2.3 Extended imaging condition 9

2.3.1 Time-lag common image gathers 12

2.3.2 Space-lag common image gathers 14

2.3.3 Common-image point gathers 14

2.4 Sensitivity to velocity errors 17

2.5 Examples 22

2.6 Conclusions 26

2.7 Acknowledgments 26

[1]CHAPTER TO BE SUBMITTED TO GEOPHYSICAL PROSPECTING

CHAPTER 3 WAVEFIELD TOMOGRAPHY USING RTM BACKSCATTERING [2] . 27
3.1 Introduction . . . 27
3.2 RTM backscattering revisited . . . 30
3.2.1 Conventional imaging condition . . . 30
3.2.2 Extended imaging condition . . . 31
3.3 Wavefield tomography with extended images . . . 34
3.3.1 Inversion with time-lag gathers . . . 35
3.3.2 Inversion with space-lag gathers . . . 39
3.4 Examples . . . 40
3.4.1 Simple model with a Gaussian anomaly . . . 47
3.4.2 Complex model based on the Sigsbee 2A velocity . . . 48
3.5 Conclusions . . . 55
3.6 Acknowledgments . . . 55
CHAPTER 4 CONCLUSIONS . . . 56
REFERENCES CITED . . . 57

[2]CHAPTER TO BE SUBMITTED TO GEOPHYSICS

LIST OF FIGURES

Figure 2.1 Synthetic model example: (a) time-lag gather at x=5km, (b) space-lag gather at x=5km, (c) common image point at x=5km, z=1.5km and (d) migrated image of one shot (in x=5km, z=0km) with receivers in the surface 6

Figure 2.2 Pictorial explanation of RTM imaging: rows 1, 2 and 3 correspond to three different snapshots at times $t_1 = 0.150s$, $t_2 = 0.275s$ and $t_3 = 0.500s$. Columns 1 to 4 correspond to the source wavefield, the receiver wavefield, the multiplication of the source and receiver wavefields, and the accumulated image over time, respectively. 10

Figure 2.3 Illustration of the linearity of the conventional imaging condition. We can split the conventional image, Figure 2.1(d), in four separate images, $R^{ff}(\mathbf{x})$ (a), $R^{fb}(\mathbf{x})$ (b), $R^{fb}(\mathbf{x})$ (c), and $R^{bb}(\mathbf{x})$ (d),corresponding to the correlation of the forward scattered and/or backscattered components of the source andreceiver wavefields 11

Figure 2.4 Illustration of the linearity of the time-lag extended imaging condition. We cansplit a time-lag gather, 2.1(a), in four separate images, $R^{ff}(z,\tau)$ (a), $R^{bf}(z,\tau)$ (b), $R^{fb}(z,\tau)$ (c) and $R^{bb}(z,\tau)$ (d), corresponding to the forward scattered and/or backscattered components of the source andreceiver wavefields 13

Figure 2.5 Illustration of the linearity of the space-lag extended imaging condition. We can divide Figure 2.1(b) in four images, $R^{ff}(z,\lambda_x)$ (a), $R^{bf}(z,\lambda_x)$ (b), $R^{fb}(z,\lambda_x)$ (c) and $R^{bb}(z,\lambda_x)$ (d), corresponding to the correlation of the forward scattered and/or backscattered components of the source andreceiver wavefields 15

Figure 2.6 Illustration of the linearity of the extended imaging condition for a common image point. We can decompose a CIP, 2.1(c), in four images $R^{ff}(\boldsymbol{\lambda},\tau)$ (a), $R^{bf}(\boldsymbol{\lambda},\tau)$ (b), $R^{fb}(\boldsymbol{\lambda},\tau)$ (c), $R^{bb}(\boldsymbol{\lambda},\tau)$ (d)corresponding to the correlation between the forward scattered and/or backscattered components of the source andreceiver wavefields 16

Figure 2.7 Model error sensitivity with time-lag gathers: (a) -12%, (b) -9%, (c) -6%,(d) -3%, (e) 0%, (f) +3%, (g) +6%, (h) +9% and (i) +12% velocity perturbationin the top layer. The maximum energy of the backscattered events occur with correct velocity shown in panel (e). . . . 18

Figure 2.8 Model error sensitivity with space-lag gathers: (a) -12%, (b) -9%, (c) -6%, (d) -3%, (e) 0%, (f) +3%, +(g) +6%, (h) +9% and (i) +12% velocity perturbation in the top layer. Note that the maximum of backscattered energy happens with the correct velocity shown in panel (e). 19

Figure 2.9 Model error sensitivity with CIP gathers: (a) -12%, (b) -9%, (c) -6%, (d) -3%, (e) +0%, (f) +3%, (g) +6%, (h) +9% and (i) +12% velocity perturbation in the top layer 20

Figure 2.10 Penalty functions for time-lag gathers (a), space-lag gathers (b) and CIP gathers. Blue and white colors represent low and high penalty, respectively. 22

Figure 2.11 Normalized objective functions for time-lag gathers J_τ (a),space-lag gathers J_{λ_x} (b) and CIP gathers $J_{\mathbf{c}}$. 23

Figure 2.12 Sigsbee 2a analysis: time-shift gather (a), space-lag gather (b), common image point (c) and RTM image (d). The vertical line and thick point shown in the RTM image shows the CIG and CIP locations respectively. . 24

Figure 3.1 Synthetic experiment setup: (a) the density (spike function) model (g/cc) and the velocity (step function) model (km/s), and (b) the modeled data. 32

Figure 3.2 Time-lag gathers for (a) low, (b) correct and (c) high velocities. 33

Figure 3.3 Space-lag gathers for (a) low, (b) correct and (c) high velocities. 35

Figure 3.4 Gradients obtained using time-lag gathers for (a)-(b) low, (c)-(d) correct, and (e)-(f) high velocities. Gradients (a), (c), and (e) are constructed without filtering and (b), (d) and (f) with filtering. 38

Figure 3.5 Gradients obtained using space-lag gathers for (a)-(b) low, (c)-(d) correct, and (e)-(f) high velocities. Gradients (a), (c), and (e) are constructed without filtering and (b), (d) and (f) with filtering. 40

Figure 3.6 (a) Gaussian velocity model, (b) starting velocity without the sharp boundary and (c) starting model with the sharp boundary. 41

Figure 3.7 (a) Conventional image from starting model in 3.6(b), and (b) its space-lag gathers. Note the structural anomaly in the middle of the image (top). Compare with Figure 3.9(a). The blue lines show the location of the gathers. 42

Figure 3.8 (a) Conventional image from starting model in 3.6(c), and (b) and its space-lag gathers. Note how the backscattering spreads the defocusing of the events in the conventional image (top). Compare with optimized image in Figure 3.10(b). 43

Figure 3.9 (a) Conventional image from inverted model without the sharp boundary, and (b) its space-lag gathers. 44

Figure 3.10 (a) Conventional image from inverted model with the sharp boundary, and (b) its space-lag gathers. 45

Figure 3.11 (a) Final inverted velocity models without the sharp boundary, and (b) with the sharp boundary. 46

Figure 3.12 (a) True velocity model, (b) migrated data using true model and (c) space-lag. 50

Figure 3.13 (a) Starting velocity model, (b) conventional image from starting model and (c) its space-lag gathers. 51

Figure 3.14 (a) Starting velocity model with sharp boundary, (b) corresponding migrated image, and (c) its space-lag gathers. Note the strong backscattering, and its spread from $\lambda_x = 0$. 52

Figure 3.15 (a) Final inverted model for conventional approach, (b) final migrated image, and (c) the corresponding space-lag gathers. 53

Figure 3.16 (a) Final inverted model with sharp boundary, (b) final migration image and (c) its corresponding space-lag gathers. Note how the backscattering energy has been optimized and placed around $\lambda_x = 0$. . . 54

LIST OF ABBREVIATIONS

Reverse time migration . . . . . RTM

Migration Velocity Analysis . . . . . MVA

Full Waveform Inversion . . . . . FWI

Center for Wave Phenomena . . . . . CWP

Differential Semblance Optimization . . . . . DSO

Conventional Imaging Condition CIC

Extended Imaging Condition . . . . . EIC

Common Image Point . . . . . CIP

ACKNOWLEDGMENTS

This project started as a test from a statement that came out from a discussion during a lecture in Paul Sava's Seismic Imaging course. We continue developing these ideas into a full project where I had to put into practice many skills. Paul Sava, my thesis advisor, guided me in the initial stages with many discussions and questions. Our weekly meetings have been very helpful and served as the ground floor for the project.

My research greatly benefited from many discussions with members and visitors of the iTeam. I particularly would like to thank Francesco Perrone, Clément Fleury and Tongning Yang for their insights about migration, migration velocity analysis and inverse theory.

I have greatly benefited from my thesis committee, maybe not much for the project, but from the courses I have taken with Yaoguo Li and Luis Tenorio. I have learned a lot from other courses, especially from Dave Hale and Ilya Tsvankin. Special thanks to Diane Witters for all the help and discussions related to the manuscript writing.

I would not be a student at CWP without everything I learned working in the years before joining the consortium. Chronologically, each mentor I had greatly improved me professionally. Big thanks to Miguel Bosch, Alexey Artyomov, Gabriel Hernández and Antoine Guitton.

Probably the most important aspect from this experience is the personal one. I have made many friends during the past 2+ years, they have been my extended family in the Rockies, many thanks to them! Finally, I want to thank my wife Carla! Her love, support and great humour have been my biggest motor.

To the memory of my father, Fanor Díaz.

CHAPTER 1

INTRODUCTION

The industry current imaging technology is mature and depends heavily on Reverse Time Migration (RTM) (Baysal et al., 1983; McMechan, 1983; Whitmore, 1983) for complex geological settings as those found in the Gulf of Mexico (GoM). However, the biggest driver for the quality of a seismic image is still the velocity model. Finding the best model is probably the most popular research topic these days.

In the literature we can find many methods to increase the focusing of seismic images. We can classify them in two big groups depending on the domain where the error is measured: data domain or image domain. Data domain methods, such as Full Waveform Inversion (Pratt, 1999; Tarantola, 1984) have demonstrated to be very good to build high resolution velocity models. However, these methods are effective only if certain conditions are met and relies mostly on the transmission components of the data. The second family, which measures the error characterizing migrated images, seeks the synchronization of wavefields at the reflector position. These methods are known as Wave Equation Migration Velocity Analysis (WEMVA) (Fliedner and Bevc, 2008; Sava and Biondi, 2004; Shen and Symes, 2008; Weibull and Arntsen, 2013; Woodward, 1992; Yang and Sava, 2011a).

Other problem in imaging, arises in presence of sharp model changes, such as sediment-salt interface. In this problem an interpreter must place the interface before continuing the velocity building process. In this settings usually the salt model is built in an iterative work flow (Ahmed et al., 2012). A key characteristic of RTM images built with such interface are the low wavenumber events, known as RTM backscattering. These events, commonly regarded as artifacts, are due to the two-way nature of the RTM wavefield extrapolation, which at the sediment-salt interface produces the reflections for both the source and receiver wavefields.

In this thesis, I analyze the kinematic signatures of such events together with the reflection information. The idea behind this analysis is that the velocity model should be built together using all available information and not separately as is done in the present. In the second chapter of this thesis I perform a sensitivity analysis of the RTM backscattering and demonstrate that it contains kinematic sensitivity. An ideal sharp boundary produces maximum energy of the RTM backscattering. Therefore, I assert that before worrying about removing the low wavenumber events from the image, one must first try to maximize it. Furthermore, the RTM backscattering could be used as a QC mechanism for placing the sediment-salt interface.

In the third chapter, I show that one could use both the reflection information and the backscattering to optimize the velocity model in an iterative model building scheme. However, such a scheme requires that both the velocity model and the sharp boundary change at each iteration. I demonstrate this work flow with two inversion examples , where I was able to predict the position of the sharp boundary based on the velocity change above it. By using both reflection and backscattering information, some cross-talk can be produced during the gradient computation. To avoid the cross-talk and to keep the gradient smooth, I propose the use of a filter based on the Poynting vectors that preserves the correlation of wavefields traveling in the same direction.

CHAPTER 2

KINEMATIC AND FOCUSING PROPERTIES OF RTM BACKSCATTERING[3]

Reverse time migration (RTM) backscattered events are produced by the cross-correlation between waves reflected from sharp interfaces (e.g. salt bodies). These events, along with head waves and diving waves, produce the so-called RTM artifacts, which are visible as low wavenumber energy on migrated images. Commonly, these events are seen as a drawback for the RTM method because they obstruct the image of the geologic structure, which is the real objective for the process. In this chapter, we perform numeric and theoretical analysis for the purpose of understanding the RTM backscattering energy in conventional and extended images. We show that the RTM backscattering contains a measure of the synchronization and focusing information between the source and receiver wavefields. We show that this synchronization and focusing information is sensitive to velocity errors; this implies that a correct velocity model produces RTM backscattering with maximum energy. Therefore, before filtering the RTM backscattered energy we should try to obtain a model that maximizes it.

2.1 Introduction

Reverse time migration (RTM) is not a new imaging technique (Baysal et al., 1983; McMechan, 1983; Whitmore, 1983). However, it was not until the late 1990s, and mainly the 2000s that computational advances allowed the geophysical community to use this technology for exploratory 3D surveys. In general, and especially in complex geological settings, RTM produces better images than other methods. Imaging methods such as Kirchhoff migration and one-way equation migration are based on approximate solutions to the wave equation. Kirchhoff migration, a high frequency asymptotic solution to the wave equation, becomes unstable for complex velocity models. This technique also fails to easy handle multipathing

[3]CHAPTER TO BE SUBMITTED TO GEOPHYSICAL PROSPECTING

and typically creates the images based on a single travel-time arrival (e.g. most energetic or first arrival). Other methods based on approximations to the wave equation, such as phase shift migration (Gazdag, 1978), rely on a v(z) earth model and further approximations are needed to account for lateral variations (Gazdag and Sguazzero, 1984). In addition to earth model considerations, one-way wave equation migration propagate the wavefields in either the upward or the downward direction; this approximation becomes inexact when the waves propagate horizontally. Therefore, this technique fails to properly handle overturning waves and reflections from steep-dip structures. RTM's propagation engine, a two-way wave equation, makes this imaging method robust and accurate because it honors the kinematics of the wave phenomena by allowing waves to propagate in all directions regardless of the velocity model or the direction of propagation. This method also takes into account, in a natural way, multipathing and reflections from steep dips.

A striking characteristic of RTM is the presence of low wavenumber events in the image that are uncorrelated with the geology. The two-way wave equation simulates scattered waves in all directions. Therefore, the imaging condition produces new events not observed in other imaging methods that correspond to the cross-correlation between diving waves, head waves and backscattered waves. The cross-correlation between the backscattered waves is more visible in presence of sharp boundaries (e.g. the top of salt) which produces strong events that mask the image of the earth reflectivity above the salt. The backscattered events are considered as noise and are normally filtered in order to get the image of earth reflectivity.

The seismic industry has dedicated effort and time developing algorithms and strategies to filter out the backscattered energy from the image. We can classify the filtering approaches in two general families: pre-imaging condition and post-imaging condition.

The pre-imaging condition family modify the wavefields (either by modeling or wavefield decomposition) in such a way that the backscattered events do not form during the imaging process. One strategy in the pre-imaging condition category is wavefield decomposition (Fei et al., 2010; Liu et al., 2011). In this method, the source and receiver wavefield are decom-

posed in upgoing and downgoing directions. In the imaging step, we cross-correlate only the wavefields that propagate in opposite directions producing an image which corresponds to the geology. The cross-correlation between wavefields traveling in parallel directions is discarded because produce events that obstructs the geology. Other pre-imaging condition approaches are performed by modifying the wave equation to attenuate the reflections coming from sharp interfaces (Fletcher et al., 2005). A similar method applicable to post-stack migration uses impedance matching at sharp interfaces (Baysal et al., 1984).

In the post-imaging family, the artifacts are attenuated by filtering. These filtering approaches are considerably cheaper because they operate in the image space and not on the wavefields. A straightforward approach is to apply a Laplacian operator to the image (Youn and Zhou, 2001); this operator acts as a high pass filter and is effective because the backscattered events have a strong low wavenumber component. A second strategy is a signal/noise separation by least squares filtering. In this case the signal is defined as the reflectivity and the noise is the backscattered energy (Guitton et al., 2007). Finally, extended imaging conditions (Rickett and Sava, 2002; Sava and Fomel, 2006; Sava and Vasconcelos, 2011) provide information about the wavefield similarity for different space and/or time lags and can also be used to discriminate the backscattered energy. Kaelin and Carvajal (2011) take advantage of the way backscattered events appear in time-lag gathers. The backscattered events map toward zero time-lag when a correct velocity model is used for imaging, whereas the primary reflections map within a limited slope range constrained by the velocity model. This difference in slope allows us to design 2D filters that preserve events within the primaries reflections range and attenuate the backscattered energy.

In this article we analyze the information carried by the backscattered energy in the extended images. We show that the backscattered waves provide important information about the synchronization between the reconstructed wavefields in the subsurface, i.e. an image obtained with a correct velocity model shows maximum backscattered energy. The presence of backscattered energy in the image not only depends on the interpretation of the

sharp interface but also on the velocity above it. We analyze the mapping patterns of the backscattered events in the extended images using wavefield decomposition approaches and conclude that backscattered energy is sensitive to the velocity model accuracy and therefore should be included as a source of information to migration velocity analysis (MVA). Counter to common practice, we assert that backscattering artifacts should be enhanced during RTM to constrain the velocity models, and they should only be removed in the last stage of imaging.

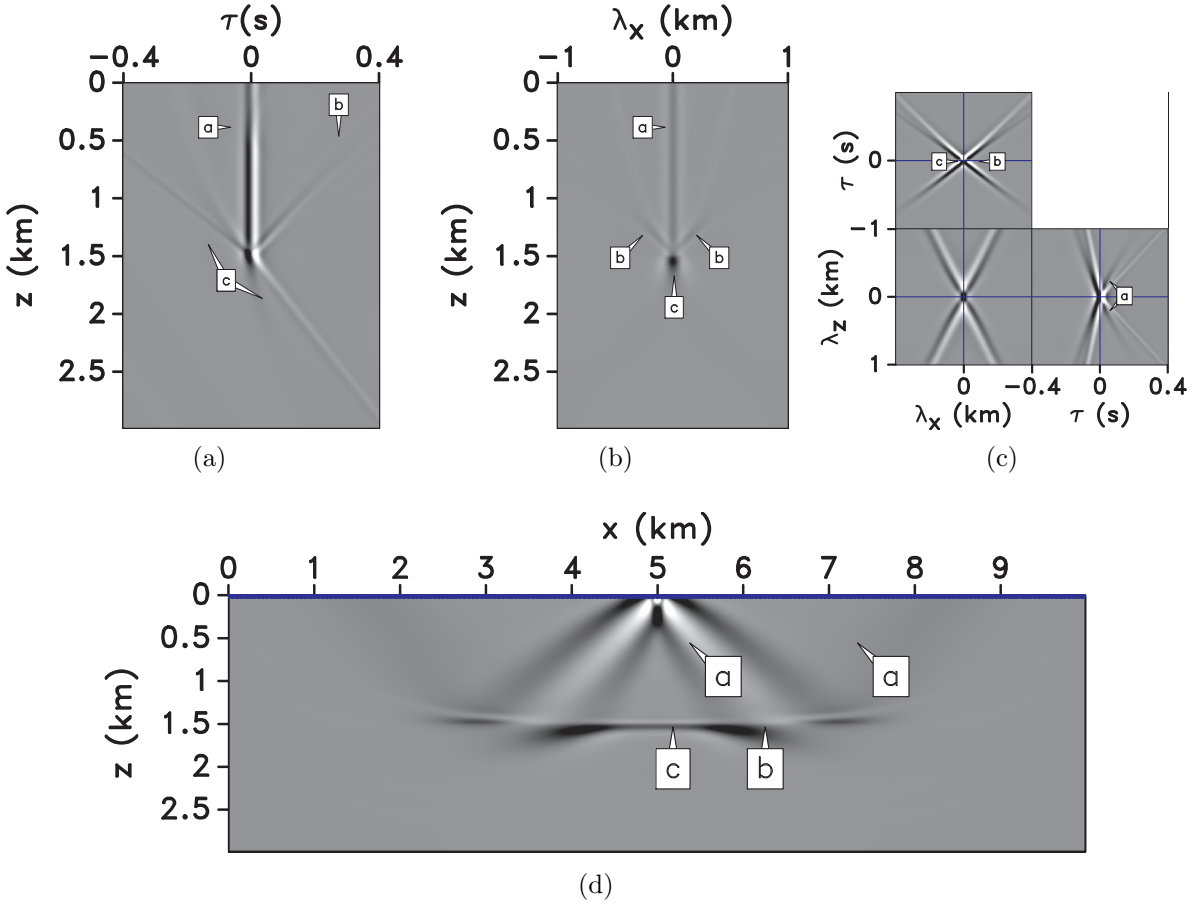


Figure 2.1: Synthetic model example: (a) time-lag gather at x=5km, (b) space-lag gather at x=5km, (c) common image point at x=5km, z=1.5km and (d) migrated image of one shot (in x=5km, z=0km) with receivers in the surface

2.2 Conventional imaging condition

The conventional imaging condition (Claerbout, 1985) is a zero time lag cross-correlation between the source wavefield and the receiver wavefields:

$$R(\mathbf{x}) = \sum_{shots} \sum_{t} u_s(\mathbf{x}, t) u_r(\mathbf{x}, t), \tag{2.1}$$

which honors the single scattering or Born assumption. Under this assumption the forward scattered source wavefield generates secondary waves as it interacts with the medium discontinuities. These secondary waves propagate in space and are recorded at the surface. This assumption means that both the source and receiver wavefields carry only transmitted energy through interfaces between layers with different elastic properties.

A wavefield extrapolated with RTM could show, depending on the complexity of the geology, waves traveling in both upward and downward directions, such as diving waves, head waves and backscattered waves. The interaction between these waves contained in the source and receiver wavefields generates new events in the image which are commonly referred to as artifacts because they do not follow the geology (i.e. earth reflectivity), which is the objective of the imaging process. The correlation between forward and backscattered waves is particularly strong when sharp boundaries are present in the velocity model (e.g. salt bodies).

If a sharp boundary is present in the model, we can decompose the source wavefield into forward scattered and backscattered energy that originates at the sharp boundary:

$$u_s(\mathbf{x}, t) = u_s^b(\mathbf{x}, t) + u_s^f(\mathbf{x}, t), \tag{2.2}$$

where the superscripts ^{b} and ^{f} stand for backscattered and forward scattered wavefield, respectively.

The same idea can be applied to the receiver wavefield:

$$u_r(\mathbf{x}, t) = u_r^b(\mathbf{x}, t) + u_r^f(\mathbf{x}, t). \tag{2.3}$$

By taking advantage of the linearity of equation 2.1, we can split the conventional imaging condition as follows:

$$R(\mathbf{x}) = R^{ff}(\mathbf{x}) + R^{bb}(\mathbf{x}) + R^{bf}(\mathbf{x}) + R^{fb}(\mathbf{x}). \tag{2.4}$$

Here, the first superscript is associated with the source wavefield and the second is associated to the receiver wavefield. For example, $R^{fb}(\mathbf{x})$ is an image constructed with the forward scattered source wavefield and the backscattered receiver wavefield.

By analyzing the individual contributions to the image, we can better understand how the backscattered events are constructed in the image. This analysis is similar to the one of Fei et al. (2010) and Liu et al. (2011) whose objective is to filter out the non-geological portions of the image. Here, we approach the problem in a broader sense by attempting to understand the physical meaning of the backscattered energy and its uses for velocity model building.

2.2.1 Backscattered events in the conventional image

In order to gain an understanding of the RTM backscattered events, we use a simple model with two-layers and strong velocity contrast. Figure 2.1(d) shows the image obtained with the conventional imaging condition for one shot at $x = 5$km. This image has strong backscattered energy, indicated with letter "a", above the reflector located at $z = 1.5$km.

To better understand the origin of the backscattered artifacts, we illustrate the wavefields used for imaging our simple model. Figures 2.2(a), 2.2(b) and 2.2(c) show three different snapshots of the source wavefield. Likewise, Figures 2.2(d), 2.2(e) and 2.2(f) show the same snapshots for the receiver wavefield. Figures 2.2(g), 2.2(h) and 2.2(i) show the product between source and receiver wavefields for the same time snapshots. Finally, Figures 2.2(j), Figure 2.2(k) and Figure 2.2(l) show the accumulated image as a function of time (integration over time of the product between wavefields).

Figure 2.2(j) shows the interaction between the forward scattered source wavefield u_s^f, shown in Figure 2.2(a), and the backscattered receiver wavefield u_r^b shown in Figure 2.2(d). In this case, the backscattered receiver wavefield travels in perfect synchronization with the forward scattered source wavefield, therefore their product, shown in Figure 2.2(g), stacks coherently in the imaging process generating the $R^{fb}(\mathbf{x})$ contribution to the image $R(\mathbf{x})$. In the $R^{fb}(\mathbf{x})$ image, the backscattered receiver wavefield behaves as the forward scattered source wavefield, which is the reason why the backscattered energy is imaged toward the source location. In the partial image at $t = 0.275$s, shown in Figure 2.2(k), we see how we start building the reflector image. The backscattered source wavefield, shown in Figure 2.2(b), generates new backscattered events corresponding to the $R^{bf}(\mathbf{x})$ image. In the snapshot at $t = 0.5$s, the reflector is completely imaged and for the remaining time we only add backscattered energy corresponding to the $R^{bf}(\mathbf{x})$ image. Here, the backscattered source wavefield behaves as the receiver wavefield and its energy maps toward the receivers. We can see that after the imaging process is finished, Figure 2.1(d), the backscattered energy is maximum near the critical angle range (where the reflected source and receiver wavefields have maximum energy).

Using wavefield decomposition allow us to isolate the individual contributions of equation 3.5. Figure 2.3(a) shows the cross-correlation between forward scattered wavefields, producing an image due to the earth reflectivity. Figures 2.3(b) and 2.3(c) show the images $R^{fb}(\mathbf{x})$ and $R^{bf}(\mathbf{x})$ corresponding to the backscattered energy, which maps toward the source and the receivers, respectively. The image corresponding to the $R^{bb}(\mathbf{x})$, shown in Figure 2.3(d), contains additional contribution to the reflectivity of the earth due to the cross-correlation between reflected wavefields. Fei et al. (2010) take advantage of this analysis to define an image free from backscattered energy as $R(\mathbf{x}) = R^{ff}(\mathbf{x}) + R^{bb}(\mathbf{x})$. Here, we want to better understand the meaning and uses of the other two partial images $R^{fb}(\mathbf{x})$ and $R^{bf}(\mathbf{x})$.

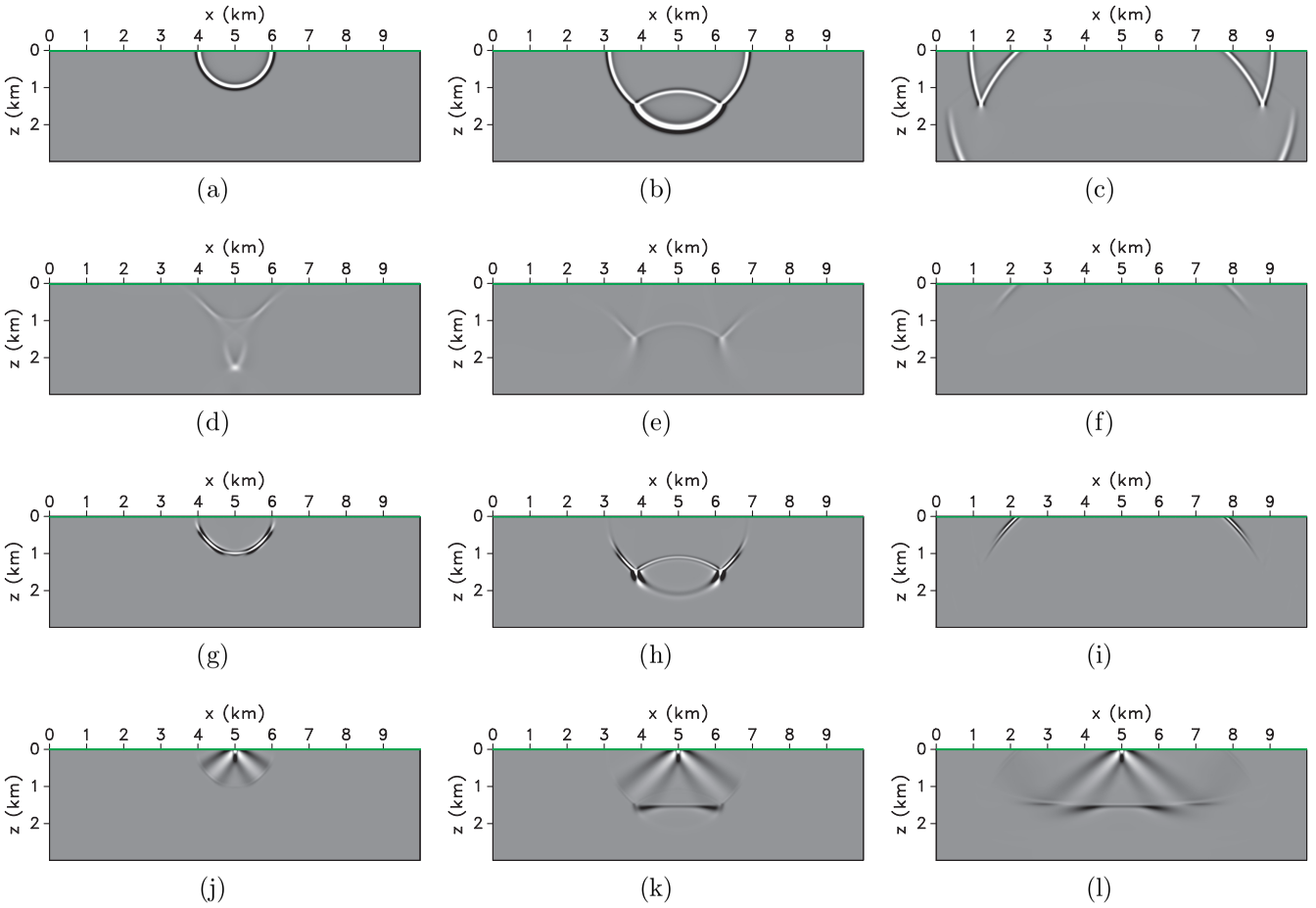
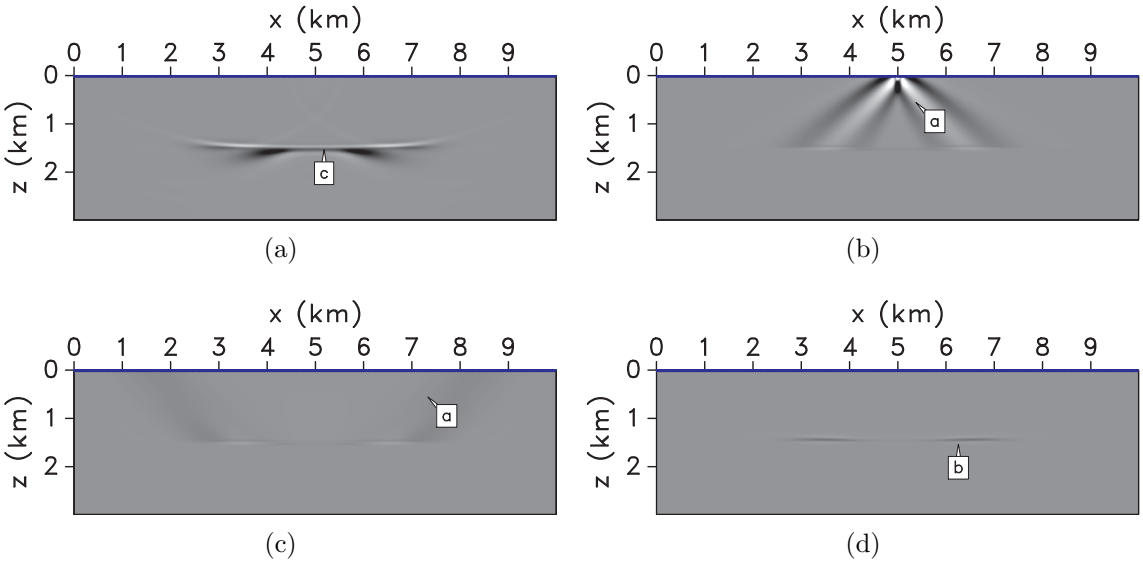


Figure 2.2: Pictorial explanation of RTM imaging: rows 1, 2 and 3 correspond to three different snapshots at times $t_1 = 0.150s$, $t_2 = 0.275s$ and $t_3 = 0.500s$. Columns 1 to 4 correspond to the source wavefield, the receiver wavefield, the multiplication of the source and receiver wavefields, and the accumulated image over time, respectively.



(a) (b) (c) (d)

Figure 2.3: Illustration of the linearity of the conventional imaging condition. We can split the conventional image, Figure 2.1(d), in four separate images, $R^{ff}(\mathbf{x})$ (a), $R^{fb}(\mathbf{x})$ (b), $R^{fb}(\mathbf{x})$ (c), and $R^{bb}(\mathbf{x})$ (d),corresponding to the correlation of the forward scattered and/or backscattered components of the source andreceiver wavefields

2.3 Extended imaging condition

The extended imaging condition (Rickett and Sava, 2002; Sava and Fomel, 2006; Sava and Vasconcelos, 2011) is similar to the conventional imaging condition except the cross-correlation lags between source and receiver wavefield are preserved in the output:

$$R(\mathbf{x}, \boldsymbol{\lambda}, \tau) = \sum_{shots} \sum_{t} u_s(\mathbf{x} - \boldsymbol{\lambda}, t - \tau) u_r(\mathbf{x} + \boldsymbol{\lambda}, t + \tau). \tag{2.5}$$

Here $\boldsymbol{\lambda}$ and τ represent the space-lags and time-lags, respectively, of the cross-correlation. The conventional image is a special case of the extended image $R(\mathbf{x}) = R(\mathbf{x}, \mathbf{0}, 0)$.

Using extended images allows to measure the accuracy of the velocity model by analyzing the moveout of the events (Yang and Sava, 2010), and we can perform transformations from the extended to the angle domain (Sava and Fomel, 2006; Sava and Vlad, 2011; Sava and Fomel, 2003). The extended images provide a measurement of the similarity between the source and receiver wavefields along space and time, so we can exploit these images to analyze and better understand the RTM backscattered events.

In equation 3.6 we observe an increase in the dimensionality of the image, from 3 to 7 dimensions, if we decide to extend the image in all directions. It is common to perform the analysis of extended images at limited locations in order to make this methodology feasible for large datasets. For cost considerations we often use an extension for common image gathers (CIG), for instance the time-lag axis (τ) or the space-lag axis (λ_x). We can also consider common image point gathers (CIP), where we fix an observation point $\mathbf{c} = (x, y, z)$ and analyze the image as a function of extensions $\boldsymbol{\lambda}, \tau$. If the dip is known, not all the space extensions, $\boldsymbol{\lambda}$, are needed.

Figures 2.1(a) to 2.1(c) show a time-lag gather, a space-lag gather, and a common image point, respectively, which represent subsets at fixed surface positions (for CIGs) or fixed space positions (for CIPs). Despite the fact that our model has only one reflector, we can identify several events in the conventional and extended images. Letter "a" indicates backscattered events, letter "b" indicates the events produced by the cross-correlation of reflected wavefields, and letter "c" indicates the cross-correlation between forward scattered wavefields.

In the presence of sharp velocity interfaces we can use the concept of equation 3.5, and construct four partial extended images:

$$R(\mathbf{x}, \boldsymbol{\lambda}, \tau) = R^{ff}(\mathbf{x}, \boldsymbol{\lambda}, \tau) + R^{bb}(\mathbf{x}, \boldsymbol{\lambda}, \tau) + R^{fb}(\mathbf{x}, \boldsymbol{\lambda}, \tau) + R^{bf}(\mathbf{x}, \boldsymbol{\lambda}, \tau). \tag{2.6}$$

2.3.1 Time-lag common image gathers

Using equation 3.7, we analyze the individual contributions for the time-lag gather shown in Figure 2.1(a). Figure 2.4(a) shows the image $R^{ff}(z, \tau)$ with a change in the slope of the events due to the abrupt velocity variation of the model. Above the reflector depth, the slope is controlled by the velocity of layer 1, whereas below the interface the slope is controlled by the velocity of layer 2. Figures 2.4(b) and 2.4(c) show the backscattered event contributions $R^{fb}(z, \tau)$ and $R^{bf}(z, \tau)$, respectively, which indicate that the backscattered

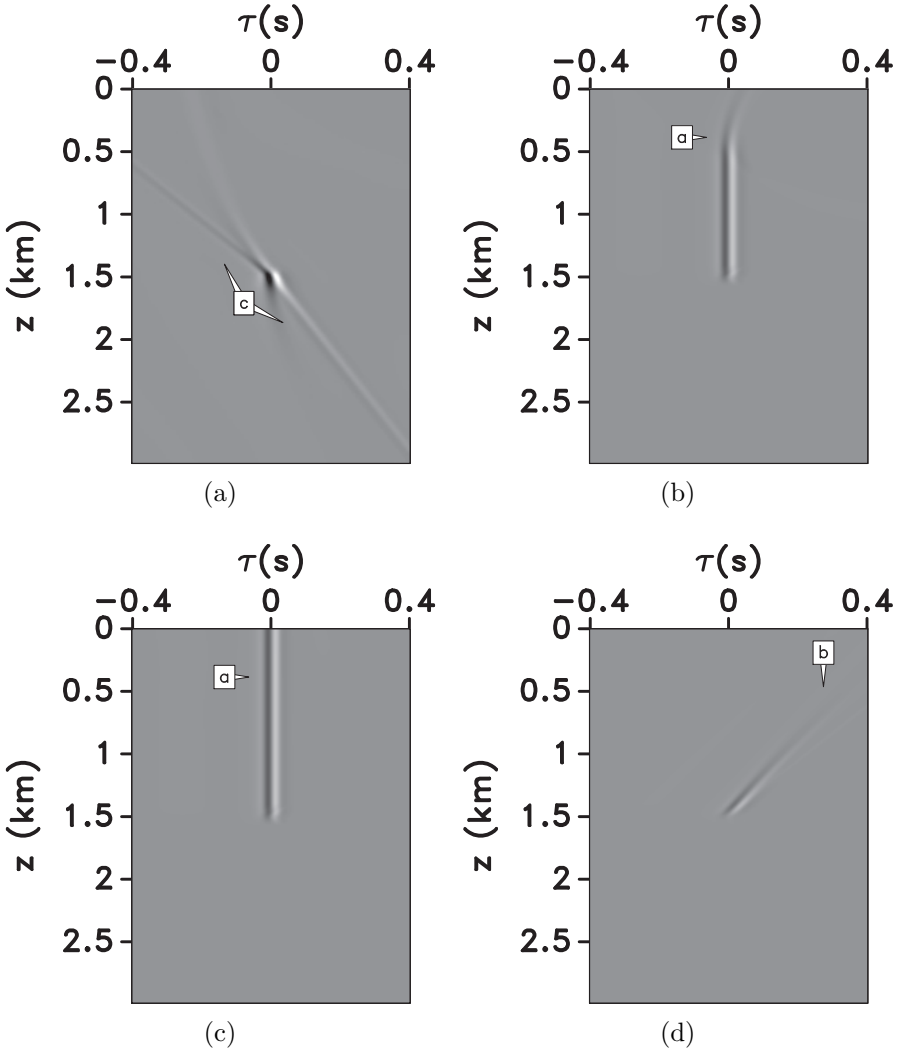


Figure 2.4: Illustration of the linearity of the time-lag extended imaging condition. We cansplit a time-lag gather, 2.1(a), in four separate images, $R^{ff}(z,\tau)$ (a), $R^{bf}(z,\tau)$ (b), $R^{fb}(z,\tau)$ (c) and $R^{bb}(z,\tau)$ (d), corresponding to the forward scattered and/or backscattered components of the source andreceiver wavefields

event maps towards τ=0 in the extended image. This means that we only get a contribution when we do not dislocate the wavefields by shifting them in time, thus reinforcing the idea of wavefield synchronization. Figure 2.4(d) shows the $R^{bb}(z,\tau)$ image; in this case the source wavefield is going in the upward direction and the receiver wavefield is going in the downward direction, which is as if we change the order of cross-correlation in equation 3.6. This is why these events map in the time-lag gathers with a slope opposite to the primary above the interface. Because the reflected waves only travel in the upper layer, we observe this image above the reflector. In the $R^{bb}(z,\tau)$ image we see two events that map with similar slope, one has the exact opposite slope as the one shown by the primary reflection, the other has a slightly higher slope (therefore indicating faster velocity) and corresponds to the interaction between head-waves produced by the velocity discontinuity and the reflected wavefields. In the time-lag gathers the slope of the primaries is very different from the backscattered events slope. Kaelin and Carvajal (2011) use the slope difference to filter the backscattered events in this domain and to extract the conventional image from the filtered extended image $R(\mathbf{x})$=$R(\mathbf{x},\tau$=0).

2.3.2 Space-lag common image gathers

Figure 2.1(b) shows a space-lag gather for the various combinations of the source and receiver wavefield components. We note that with the correct velocity model, both primaries and backscattered events map to $\lambda_x = 0$ since the velocity used for imaging is correct. Figure 2.5(a) shows the $R^{ff}(z,\lambda_x)$ image with the energy correctly focused at $\lambda_x = 0$. Figures 2.5(c) and 2.5(b) show the backscattered events $R^{bf}(z,\lambda_x)$ and $R^{fb}(z,\lambda_x)$ in the space-lag gathers, which also map toward $\lambda_x = 0$. Figure 2.5(d) shows the image coming from the reflected wavefields $R^{bb}(z,\lambda_x)$; in this case the events are visible only above the reflector because the waves travel only in the first layer.

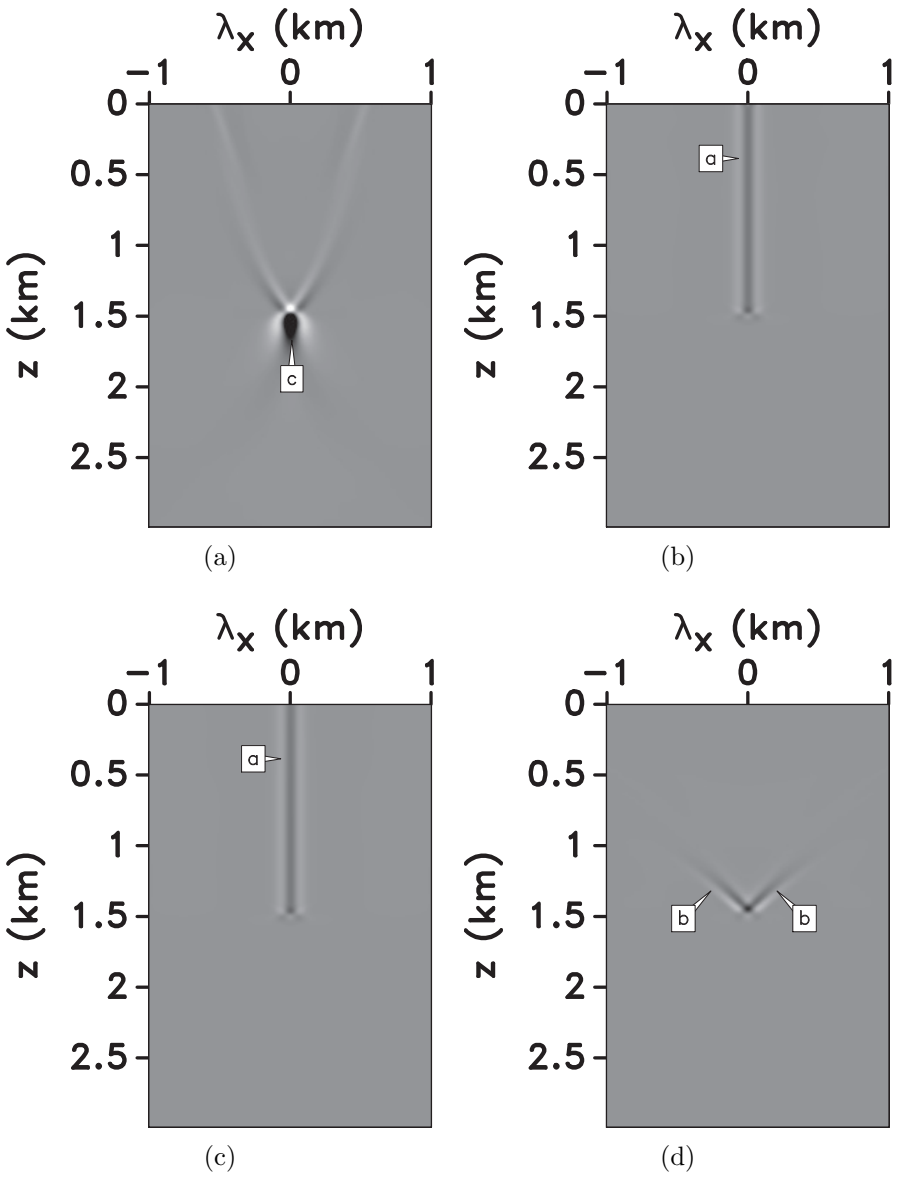


Figure 2.5: Illustration of the linearity of the space-lag extended imaging condition. We can divide Figure 2.1(b) in four images, $R^{ff}(z, \lambda_x)$ (a), $R^{bf}(z, \lambda_x)$ (b), $R^{fb}(z, \lambda_x)$ (c) and $R^{bb}(z, \lambda_x)$ (d), corresponding to the correlation of the forward scattered and/or backscattered components of the source andreceiver wavefields

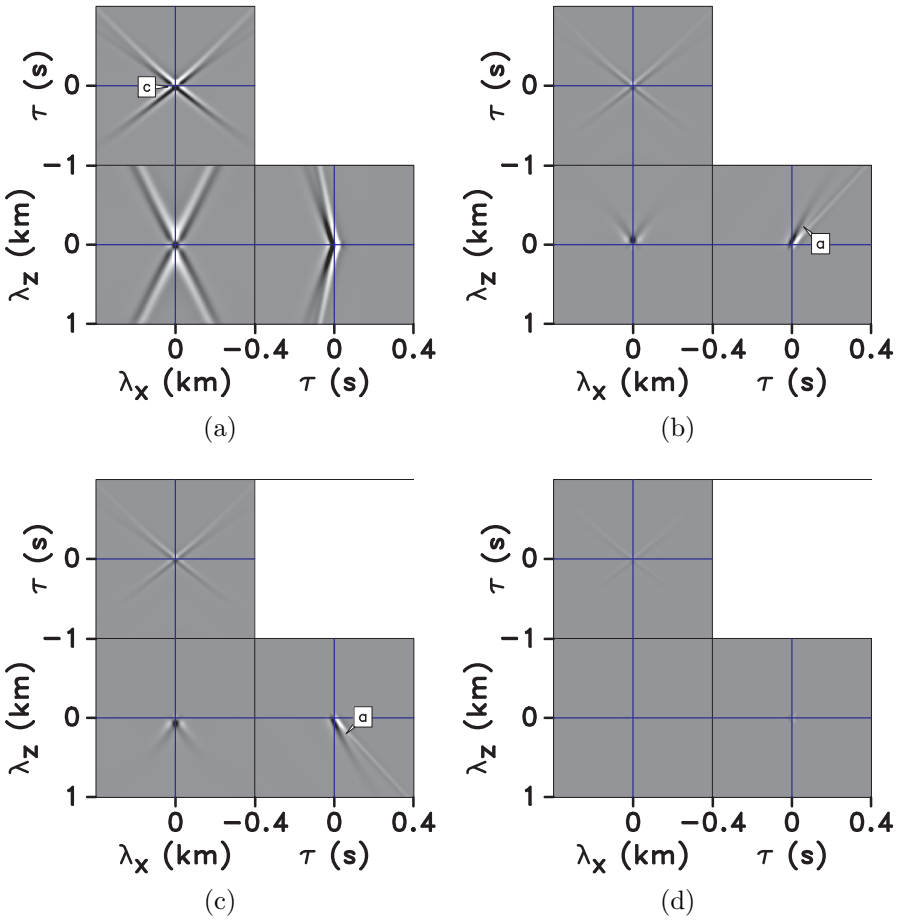


Figure 2.6: Illustration of the linearity of the extended imaging condition for a common image point. We can decompose a CIP, 2.1(c), in four images $R^{ff}(\boldsymbol{\lambda}, \tau)$ (a), $R^{bf}(\boldsymbol{\lambda}, \tau)$ (b), $R^{fb}(\boldsymbol{\lambda}, \tau)$ (c), $R^{bb}(\boldsymbol{\lambda}, \tau)$ (d)corresponding to the correlation between the forward scattered and/or backscattered components of the source andreceiver wavefields

2.3.3 Common-image point gathers

The events involving backscattered energy are also visible in CIP gathers. Figure 2.1(c) shows a CIP extracted at $\mathbf{c}$=$(5, 1.5)km$. Figure 2.6(a) shows the CIP for the forward scattered wavefields $R^{ff}(\mathbf{x}, \boldsymbol{\lambda}, \tau)$. The energy focuses at zero lag for the $\tau - \lambda_x$ panel. The $\lambda_z - \tau$ shows a kink produced by the abrupt change in velocity for the primaries, which are mapped at negative τ. Figure 2.6(b) shows the $R^{fb}(\mathbf{x}, \boldsymbol{\lambda}, \tau)$ image, and we can see a change in the $\lambda_z - \tau$ plane, where the backscattered energy is mapped to positive lags. Figure 2.6(c) shows the complementary backscattered energy that is mapped to negative λ_z and positive τ lags. The CIP from the reflected wavefields, Figure 2.6(d), shows weak energy concentrated at zero lags.

2.4 Sensitivity to velocity errors

In the previous sections we have explained the concept of wavefield synchronization for correct velocity, which implies that for correct velocity the backscattered energy maps toward zero lags. Here, we analyze the behavior of backscattered events in the presence of velocity errors. We test the sensitivity of the backscattered events with the same synthetic data discussed previously. In this case, we construct the images with different models characterized by a constant error varying from -12% to +12% in layer 1. We keep the interface consistent with the velocity used for imaging, i.e. we assume that the interface producing backscattered energy is placed in the model according to the velocity in layer 1. Figures 2.7(a) to 2.7(i) show time-lag gathers as a function of the velocity error. The backscattered energy is still mapped vertically, but away from τ=0. The backscattered events in the time-lag gathers show a kinematic error, i.e. these events move from positive τ for negative errors to negative τ values for positive errors. Figures 2.8(a) to 2.8(i) show a similar display for space-lag gathers. In this case, both, backscattered and primary energy map away from λ_x=0 when we introduce an error in the model. In space-lag gathers, the backscattered energy maps symmetrically away from zero lag with incorrect velocities. Finally, Figures 2.9(a) to 2.9(i) show

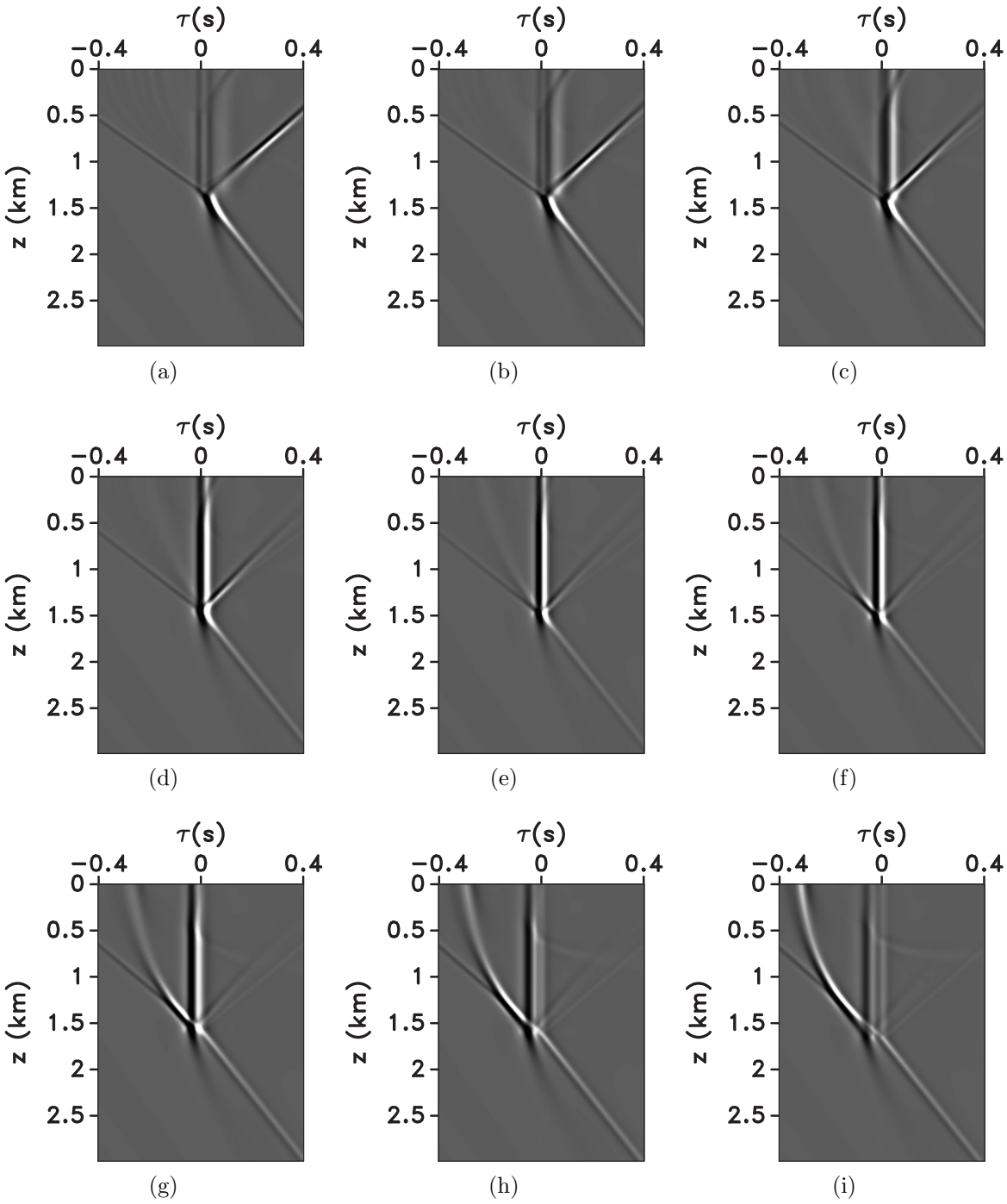


Figure 2.7: Model error sensitivity with time-lag gathers: (a) -12%, (b) -9%, (c) -6%,(d) -3%, (e) 0%, (f) +3%, (g) +6%, (h) +9% and (i) +12% velocity perturbationin the top layer. The maximum energy of the backscattered events occur with correct velocity shown in panel (e).

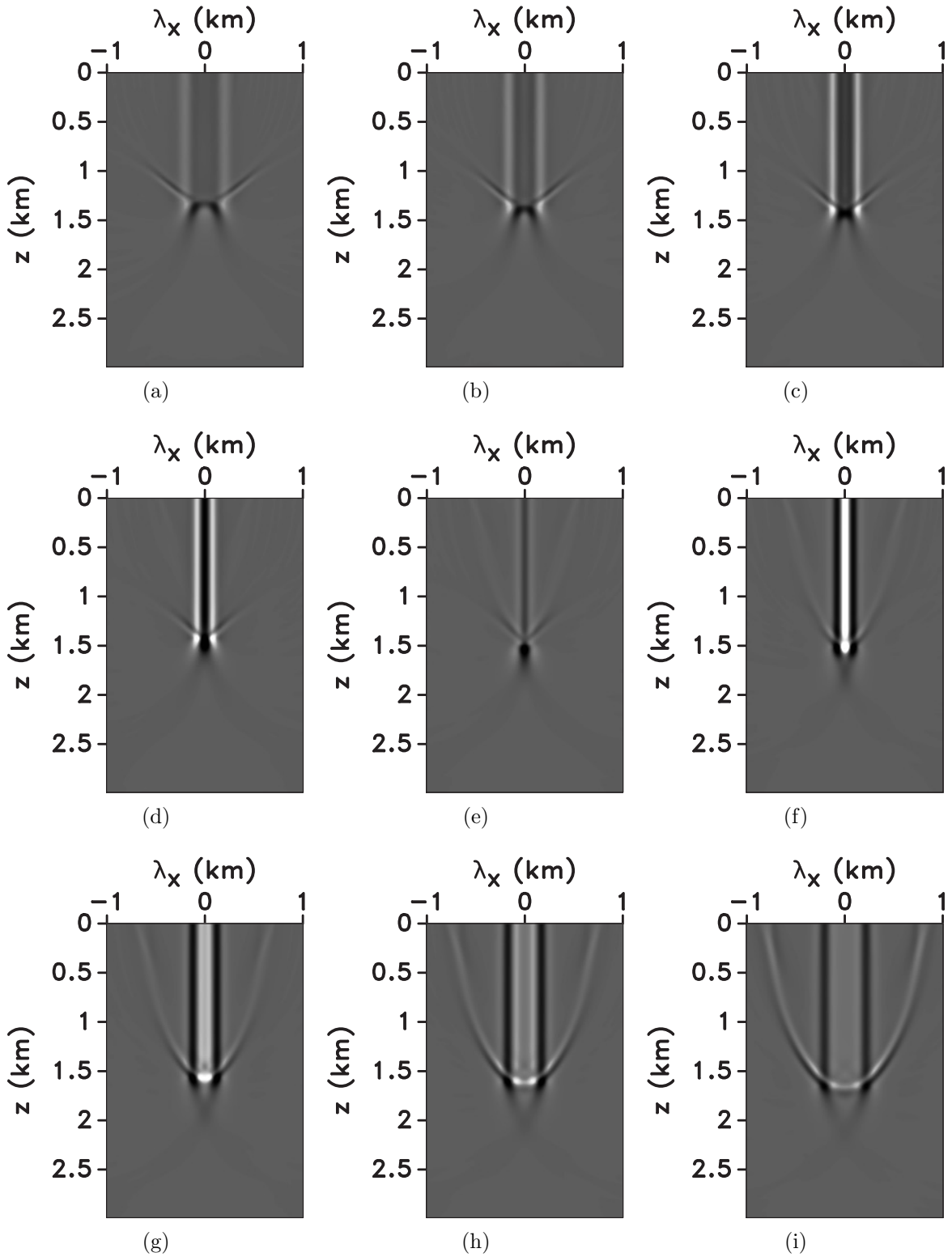


Figure 2.8: Model error sensitivity with space-lag gathers: (a) -12%, (b) -9%, (c) -6%, (d) -3%, (e) 0%, (f) +3%, +(g) +6%, (h) +9% and (i) +12% velocity perturbation in the top layer. Note that the maximum of backscattered energy happens with the correct velocity shown in panel (e).

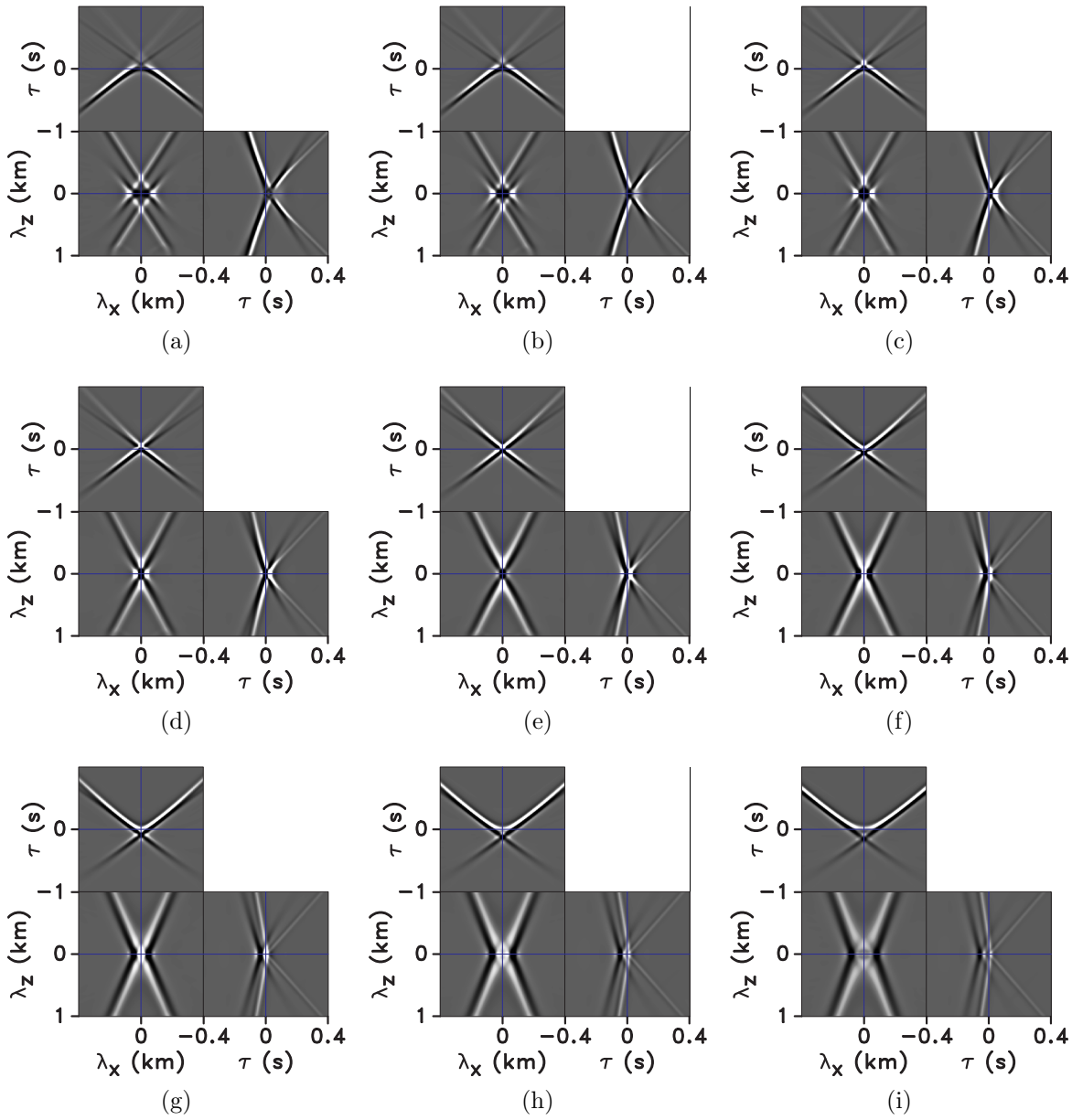


Figure 2.9: Model error sensitivity with CIP gathers: (a) -12%, (b) -9%, (c) -6%, (d) -3%, (e) +0%, (f) +3%, (g) +6%, (h) +9% and (i) +12% velocity perturbation in the top layer

the sensitivity of CIPs to velocity errors. For incorrect velocity, the events move away from zero-lags. In the CIPs, even when constructed with incorrect velocity, the primary reflections go through zero-lag, and the events in the $\tau - \lambda_x$ plane show moveout (i.e. the energy not mapped symmetrically respect zero lag). The velocity errors split the backscattered energy in the $\lambda_z - \tau$ plane, some of the energy goes through zero space-lag while other part of the energy does not. We could use the information contained in the extended images to design objective functions (OF) that exploit the presence of backscattered events. Minimizing such OF, e.g. by wavefield tomography, optimizes the sharp interface positioning (e.g. the top of salt) and the sediments velocity above it. A straightforward approach based on differential semblance optimization (Shen et al., 2003) can be adapted to use the backscattered energy seen away from zero lags by defining the objective functions for time-lag gathers

$$J_\tau = \frac{1}{2}\|P(\tau)\left[R^{fb}(\mathbf{x},\tau) + R^{bf}(\mathbf{x},\tau)\right]\|_2^2, \tag{2.7}$$

and for the space-lag gathers,

$$J_{\lambda_x} = \frac{1}{2}\|P(\lambda_x)\left[R^{fb}(\mathbf{x},\lambda_x) + R^{bf}(\mathbf{x},\lambda_x)\right]\|_2^2. \tag{2.8}$$

Here $P(\tau) = |\tau|$ and $P(\lambda_x) = |\lambda_x|$ are functions that penalize the backscattered energy away from zero lags, thus defining the residual that we need to minimize through inversion.

For common image points we can use the objective function

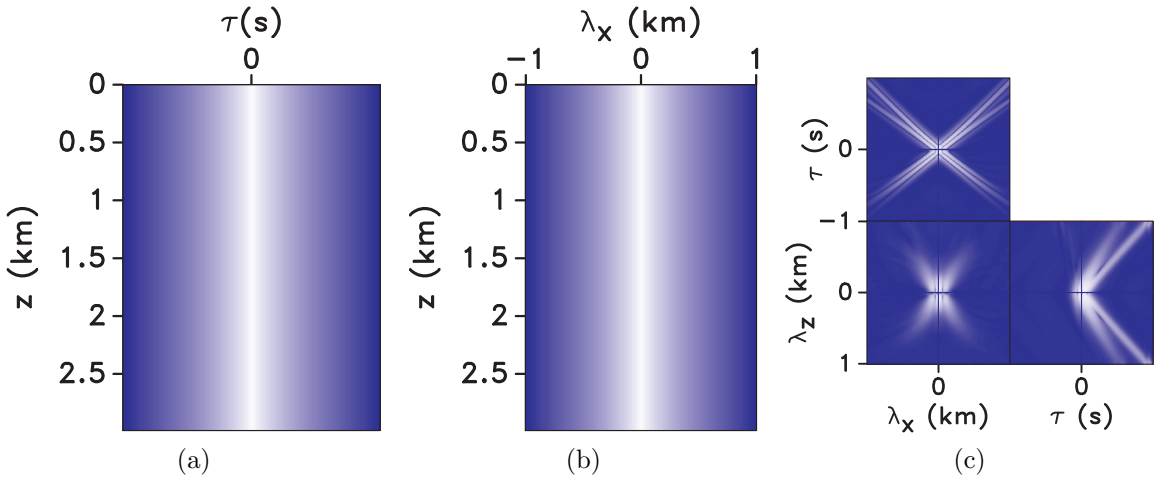
$$J_{\mathbf{c}} = \frac{1}{2}\|P(\boldsymbol{\lambda},\tau)\left[R^{fb}(\boldsymbol{\lambda},\tau) + R^{bf}(\boldsymbol{\lambda},\tau)\right]\|_2^2. \tag{2.9}$$

Here, $P(\boldsymbol{\lambda},\tau)$ is the penalty function for CIPs.

The penalty function is designed to measure the deviation or error between actual extended images and our notion for correct extended images. For CIGs we have a definite criterion, we know that the backscattered energy has to map to zero lag, that is why we can use the absolute value as penalty function. However, for CIPs the penalty operator is more complex. We use the correct CIP as reference for constructing the penalty function $P(\boldsymbol{\lambda},\tau)$ similar to the one proposed by (Yang et al., 2013). The correct CIP, shown in Figure 2.1(c)

has the right focusing within the acquisition limitations. More generally, we could use a demigration/migration process to assess correct focusing at a given CIP position, and to infer the shape of the penalty operator.

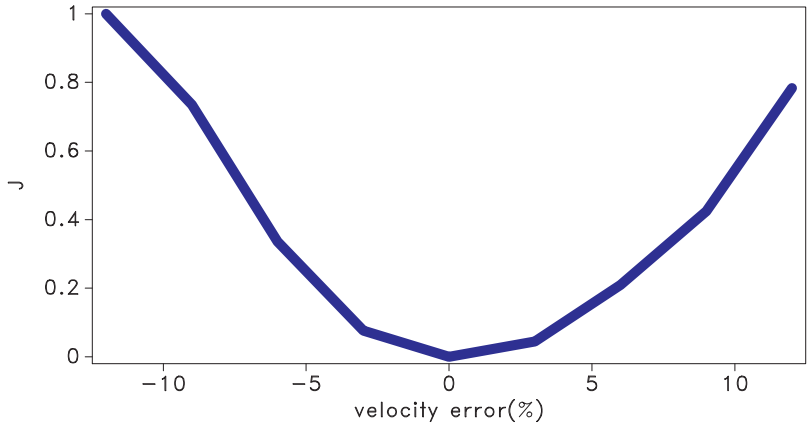
Figures 2.10(a) to 2.10(c) show the penalty functions for time-lag, space-lag and CIP gathers respectively. The objective functions for our synthetic example are shown in Figures 2.11(a) to 2.11(c) for time-lag gathers, space-lag gathers and common image point gathers respectively. One can see that in all three cases the OF minimizes at the correct model. If we want to optimize the model such that we maximize the backscattered events we need to consider two variables: the velocity model and the interface geometry. In our example the sharp interface depends linearly with the velocity model.



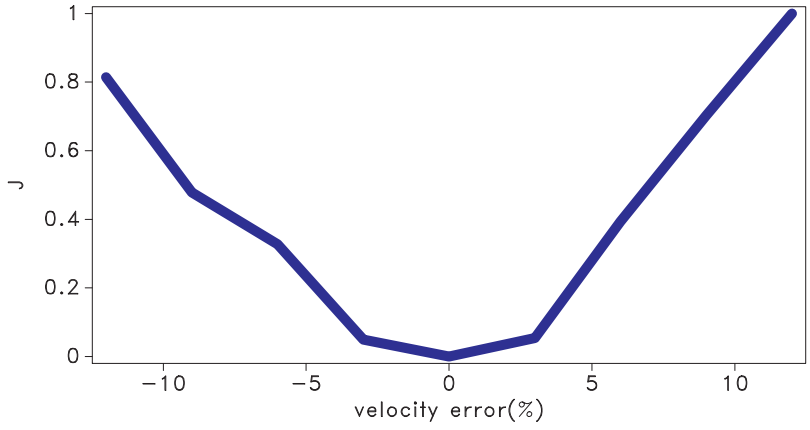
(a) (b) (c)

Figure 2.10: Penalty functions for time-lag gathers (a), space-lag gathers (b) and CIP gathers. Blue and white colors represent low and high penalty, respectively.

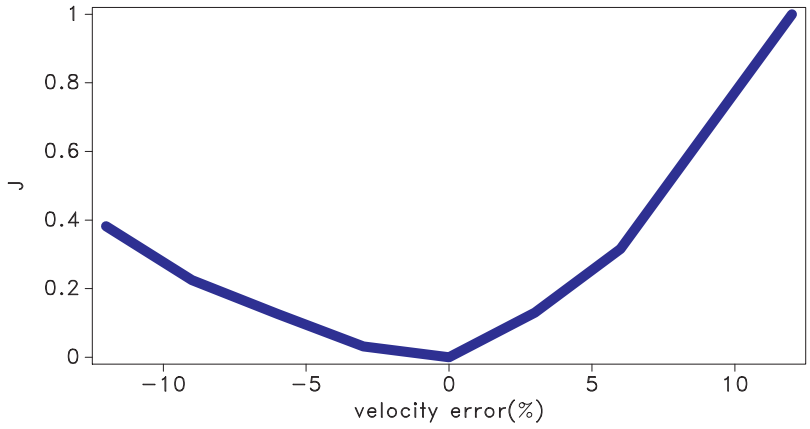
The objective functions for CIGs are shown in Figures 2.11(a) and 2.11(b) for time-lag gathers and space-lag gathers respectively. One can see that the functions minimize at the correct velocity model. In the definition of the OF we only use the backscattered energy $R^{fb}(z,\tau) + R^{bf}(z,\tau)$ and $R^{fb}(z,\lambda_x) + R^{bf}(z,\lambda_x)$ for time-lag and space. We separate the wavefield contribution using wavefield up and down decomposition, alternatively we could use slope filtering in the extended images. This is a robust and cost effective operation since



(a)



(b)



(c)

Figure 2.11: Normalized objective functions for time-lag gathers J_τ (a),space-lag gathers J_{λ_x} (b) and CIP gathers $J_{\mathbf{c}}$.

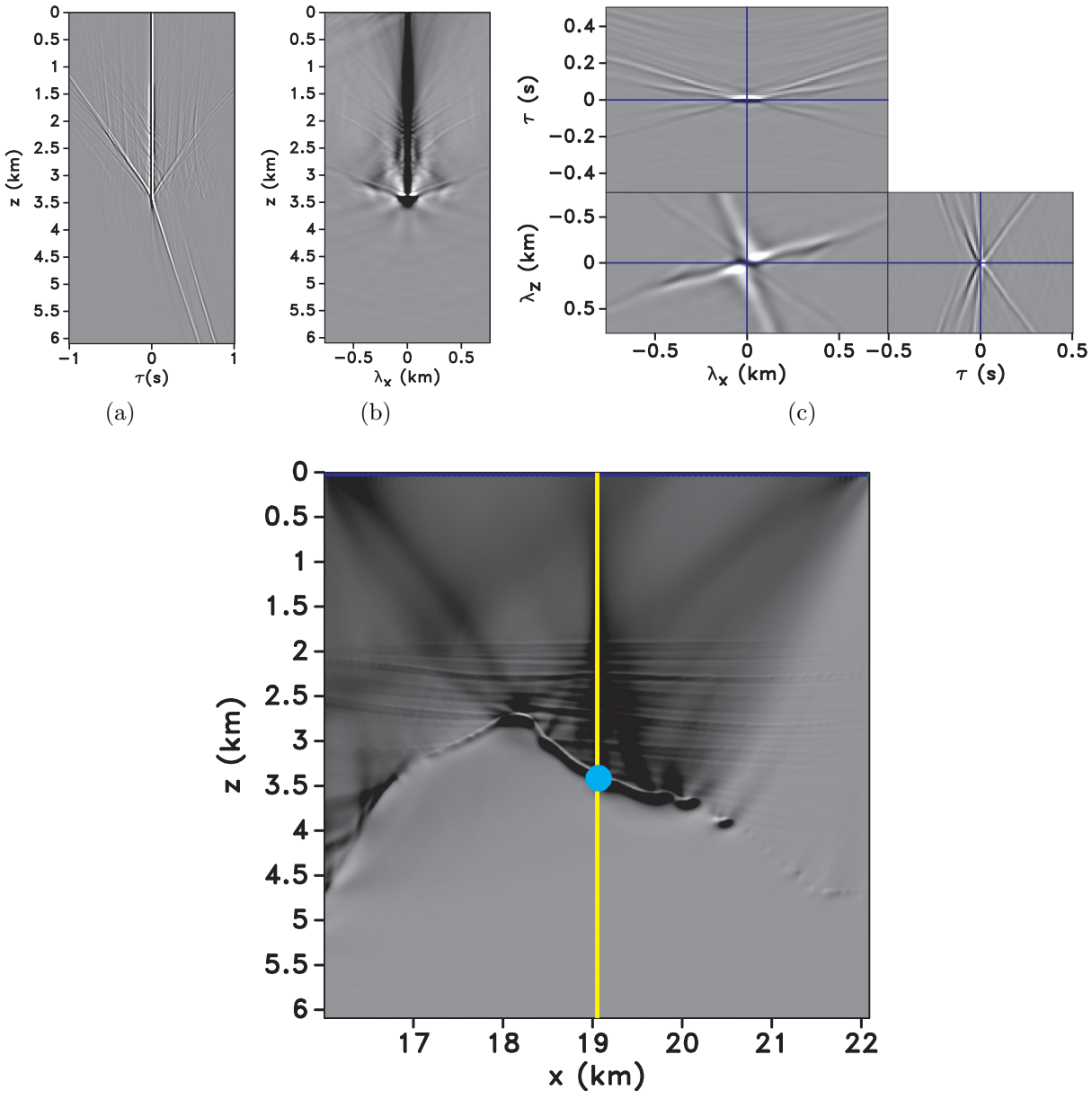
the various events in the gathers are characterized by distinct slopes as shown by Kaelin and Carvajal (2011).

2.5 Examples

In this subsection we illustrate the backscattered events visible on extended images constructed based on a modified Sigsbee 2A model (Paffenholz et al., 2002). We modify the model by salt flooding (extending the salt to the bottom of the model) to avoid backscattering from the base of salt, therefore we focus on the reflections from the top of salt only. For this example we fix the receiver array on the surface, and we use 100 shots evenly sampled on the surface to build the image. For the migration model we use the stratigraphic velocity which shows sharp interfaces in the sediment subsection, in addition the interface corresponding with the top of salt. Figure 2.12(d) shows the conventional image for our modified Sigsbee model, note the strong backscattered energy above the salt.

Figure 2.12(a) shows a time-lag gather calculated at x=19.05km. We can see that the gather is very complex, but we can easily identify the backscattered energy indicated with letter "a" in Figure 2.1(a). In this case, the backscattered energy maps directly to $\tau = 0$ because we use the correct velocity model. We can also identify the events corresponding to the cross-correlation between reflected waves from the source and receiver side $R^{rr}(z, \tau)$, indicated with letter "b". The $R^{rr}(z, \tau)$ events have positive slope (given by the sediment velocity at the interface) and are visible for $\tau > 0$. We can also observe a abrupt change in the slope of the primary reflection corresponding the sediment-salt interfaces at the top of salt indicated with letter "c".

Figure 2.12(b) shows a space-lag common image gather extracted at the same location. The backscattered energy maps toward $\lambda_x = 0$, indicated with letter "a". We see again the $R^{rr}(z, \lambda_x)$ case, indicated with letter "b", where the energy is mapped away from zero lag. Even though we are using the correct model, we still see energy away from $\lambda_x = 0$. This indicates that additional processing is needed before we can use space-lag gathers for model update with wave equation tomography.



(a) (b) (c)

(d)

Figure 2.12: Sigsbee 2a analysis: time-shift gather (a), space-lag gather (b), common image point (c) and RTM image (d). The vertical line and thick point shown in the RTM image shows the CIG and CIP locations respectively.

Figure 2.12(c) shows a common image point extracted at the top of salt interface at $(x, z) = (19.05, 3.4)$km. Despite the complexity of this image, we can still identify similar patterns as shown in Figure 2.1(c). The backscattered events are mapped to $\tau > 0$ in the $\tau - \lambda_z$ plane, indicated with letter "a". In this plane we can separate with the individual contributions from $R^{tr}(\mathbf{x}, \boldsymbol{\lambda}, \tau)$ (which maps to $\lambda_z < 0$ and $\tau > 0$), and $R^{rt}(\mathbf{x}, \boldsymbol{\lambda}, \tau)$ (which maps to $\lambda_z > 0$ and $\tau > 0$), because they are imaged into two different events, whereas in the common image gathers discussed before we cannot differentiate the individual contributions, because both cases map to zero lag. The image of the reflector maps as a point to zero lag in the $\tau - \lambda_x$ plane (indicated with letter "c").

Understanding the backscattered energy in the extended images for complex scenarios is the first step in using these events for migration velocity analysis. In this article, we used wavefield decomposition to analyze the patterns of the backscattered energy in conventional and extended images. Although effective, wavefield decomposition can be very costly, specially for 3D models. In practice we need to use filtering of the extended images to isolate the events corresponding to the backscattered energy.

2.6 Conclusions

RTM backscattered energy is produced by the correlation of waves originating at sharp boundaries (e.g. salt bodies) contained in the model. The two-way wave equation operator allows waves to travel in all directions for both the source and the receiver wavefiels. Therefore, during the imaging condition (conventional or extended) we obtain events that contribute to the reflectivity and events that produce RTM backscattering for different source and receiver wavefields combination. The specific combinations that produce RTM backscattering indicate the synchronization between wavefields along the wavepaths that connect the source with the subsurface and the subsurface with the receivers. We demonstrate that the RTM backscattered energy is sensitive to kinematic errors in the velocity model. Hence, a correct velocity model produces maximum synchronization or focusing along the incident and reflected wavepaths. The backscattered energy in the final image should not be considered as

an artifact or a drawback of the imaging method; rather, the backscattered energy should be maximized in the image in order to ensure an optimum velocity model. The synchronization and focusing observations drawn in this paper demonstrate that the backscattering carries kinematic information that can be used during tomographic updates.

2.7 Acknowledgments

I would like to thank to Mariana Carvalho and Tongning Yang for insightful discussions with the common image point gathers analysis.

CHAPTER 3

WAVEFIELD TOMOGRAPHY USING RTM BACKSCATTERING [4]

Reverse time migration (RTM) backscattering contains kinematic information that can be used to constrain velocity models. The backscattering results from the correlation between forward scattered and backscattered wavefields from sharp interfaces, i.e. sediment-salt interfaces. The synchronization between these wavefields depends on the velocity of the sediment section and the correct interpretation of the sharp boundary. We propose an optimization workflow where both the sediment velocity and the sharp boundary are updated iteratively. The presence of sharp boundaries in the model leads to high and low wavenumber components in the objective function gradient; the high wavenumber components correspond to the correlation of wavefields traveling in opposite directions, whereas the low wavenumber components correspond to the correlation of wavefields traveling in the same direction. This is behavior is similar to reverse-time migration where the high wavenumber components represent the reflectors (the signal) and the low wavenumber components represent backscattering (noise). The opposite is true in tomography: the low wavenumber components represent changes to the velocity model and the high wavenumber components are noise that needs to be filtered out. We use a directional filter based on Poynting vectors during the gradient computation to preserve the smooth components of the gradient thus spreading information away from the sharp boundary. Our tests indicate that velocity models are better constrained when we include the sharp boundaries (and the associated backscattering) in wavefield tomography.

3.1 Introduction

The two-way way equation is the engine of reverse-time migration (RTM) (Baysal et al., 1983; McMechan, 1983; Whitmore, 1983). This imaging technology is used routinely to obtain high fidelity images of the subsurface. Despite the computing cost, the two-way

[4]CHAPTER TO BE SUBMITTED TO GEOPHYSICS

operator has many advantages over other modeling approaches, like downward continuation or Kirchhoff modeling. This technique is especially suited for complex geological settings such as those with strong velocity gradients, sharp boundaries (e.g. salt bodies), and strong lateral variations. The reason for the RTM success is that a wavefield reconstructed with the two-way operator can easily handle any dip, multi-pathing, and reflections from steep structures (Etgen et al., 2009; Gray et al., 2001).

RTM also produces low wave-number events in seismic images, which are usually referred to as RTM artifacts. The low wave-number energy is produced by the correlation of waves that propagate in the same direction, thus violating the assumptions of the conventional cross correlation imaging condition (Claerbout, 1971). Such events include backscattered waves, head-waves, and diving waves. The backscattered events obstruct the image representing the subsurface reflectivity, and so are usually considered noise. Numerous techniques can be employed to remove the RTM noise. In terms of filtering approach, we could divide such methods in two categories: pre-imaging filtering (Fletcher et al., 2005; Liu et al., 2011; Yoon et al., 2004) and post-imaging filtering (Guitton et al., 2007; Kaelin and Carvajal, 2011; Youn and Zhou, 2001; Zhang and Sum, 2009). For detailed analysis of RTM backscattering events, the reader is referred to Díaz and Sava (2012).

Although the low wavenumber energy is noise for imaging purposes, it can be used for velocity model-building. This energy is the result of the correlation of waves traveling in the same direction, thus coinciding in space and time. This space and time coincidence only occurs when the wavefields extrapolation is accurate. Therefore, if the velocity model is correct, the RTM backscattering is strong simply because the wavefields are synchronized (Díaz and Sava, 2012). For reflected data, the space-time synchronization criterion also applies at the reflector position. Since both types of waves (transmitted and reflected) share the same kinematic behaviour, we can design a joint optimization problem that improves the synchronization of all the data simultaneously, thus allowing us to refine the model and to use the RTM backscattering as a source of information instead of treating it as noise.

To optimize the velocity model, one can choose a method that is consistent with the modeling operator (two-way). Such an inverse problem could be formulated by finding a model that produces data which resembles the observed data, as is done in Full Waveform Inversion (Pratt, 1999; Tarantola, 1984). This data-domain approach relies on the kinematic and dynamic consistencies between modeled and observed data. Therefore, if the propagation engine used is not dynamically consistent with the data, i.e. the modeled amplitudes are not accurate, then the chances for convergence diminish. Alternatively, one can optimize the model in the image space using techniques from the family usually referred to as wavefield tomography (Fliedner and Bevc, 2008; Sava and Biondi, 2004; Shen and Symes, 2008; Woodward, 1992; Yang and Sava, 2011a). The image domain approach seeks the kinematic synchronization of the wavefields at an image location. Therefore, the aim of this method is to improve the image focusing rather than to match the dynamic information of the wavefields as in done in the data-domain approach. This increases the robustness of the method, but decreases its ability to construct high resolution models.

One way to formulate the problem in the image space is by using extended images (Rickett and Sava, 2002; Sava and Fomel, 2006; Sava and Vasconcelos, 2011), from which we can extract wavefield similarities in space and time (Shen et al., 2003; Weibull and Arntsen, 2013; Yang and Sava, 2010). Extended images are normally used for optimizing the reflected data information, but Díaz and Sava (2012) show that similar to reflected data, the RTM backscattered energy also maps to zero time-lag and space-lag when the velocity model is correct.

In this paper, we demonstrate that it is possible to use the backscattered waves for image-domain wavefield tomography. Using the two-way wave equation operator allows simultaneous inversion based on the reflected and backscattered waves. We formulate the tomography problem using the adjoint state method (ASM), which is an efficient technique for gradient-based optimization (Plessix, 2006). However, the gradient computed using the ASM suffers from cross-talk between forward and backscattered waves, which produces un-

desirable reflector-like events. In order to avoid the unwanted correlations, we apply a directional filter designed to keep the contributions between wavefields traveling in the same direction during the correlation step of the gradient computation. This filter is based on the Poynting vectors of the extrapolated wavefields (Yoon et al., 2004), although other filtering techniques can be used instead.

We start this paper with a brief review of the RTM backscattering kinematic properties and the mapping patterns in extended images, and then we review wavefield tomography using extended images. We show how this methodology can be adapted to backscattering energy and define an objective function and its gradient, which are essential for inversion. We then illustrate how we can make use of the backscattering information for wavefield tomography, and demonstrate our method using a complex synthetic based on the Sigsbee model (Paffenholz et al., 2002).

3.2 RTM backscattering revisited

RTM backscattering is produced in the presence of sharp models, e.g. sediment-salt interfaces. In such cases, wavefields extrapolated with a two-way operator (e.g. the scalar wave equation)

$$\frac{1}{v_p^2(\mathbf{x})}\frac{\partial^2 u(\mathbf{x},t)}{\partial t^2} - \nabla^2 u(\mathbf{x},t) = f(\mathbf{x},t) \tag{3.1}$$

contains forward and backscattered components. Here, $u(\mathbf{x},t)$ the reconstructed wavefield, $v(\mathbf{x})$ the medium velocity and $f(\mathbf{x},t)$ the source function. Therefore, we can write the source wavefield as a superposition of two components

$$u_s(\mathbf{x},t) = u_s^b(\mathbf{x},t) + u_s^f(\mathbf{x},t), \tag{3.2}$$

where the superscripts ^{b} and ^{f} correspond to the backscattered and forward scattered wavefields from the sharp boundary, respectively. Similarly, the receiver wavefield can be decomposed into two components with the equivalent naming convention:

$$u_r(\mathbf{x},t) = u_r^b(\mathbf{x},t) + u_r^f(\mathbf{x},t). \tag{3.3}$$

3.2.1 Conventional imaging condition

The source and receiver wavefields allow one to construct an image with the conventional imaging condition (Claerbout, 1971) defined as the zero-lag correlation between source and receiver wavefields:

$$R(\mathbf{x}) = \sum_e \sum_t u_s(e, \mathbf{x}, t) u_r(e, \mathbf{x}, t). \tag{3.4}$$

Here e refers to the experiment index, e.g. shot number or plane-wave take-off angle.

If the wavefields used in imaging contain backscattering, we can substitute equations 3.2 and 3.3 into equation 3.4 and obtain an image which is a superposition of 4 individual images:

$$\begin{aligned} R(\mathbf{x}) = R^{ff}(\mathbf{x}) + R^{bb}(\mathbf{x}) \\ + R^{bf}(\mathbf{x}) + R^{fb}(\mathbf{x}). \end{aligned} \tag{3.5}$$

Following the convention in Díaz and Sava (2012), the first superscript corresponds to the source wavefield and the second to the receiver wavefield. In this total image, two components (^{ff} and ^{bb}) provide an estimate of the reflectivity, and the other two components (^{fb} and ^{bf}) represent backscattering. This means that the backscattering is produced from the correlation of wavefields traveling in the same direction. For example, $R^{bf}(\mathbf{x})$ is produced when the backscattered source wavefield $u_s^b(\mathbf{x}, t)$ resembles the forward scattered receiver wavefield $u_r^f(\mathbf{x}, t)$, and $R^{fb}(\mathbf{x})$ is produced with the opposite combination of the propagating wavefields. Several authors (Fei et al., 2010; Liu et al., 2011; Yoon et al., 2004) use this wavefield directionality notion to keep only the components related to reflectivity in the image and to remove everything else. Here we use the directionality concept to keep the components that travel in the same direction during tomography.

3.2.2 Extended imaging condition

A generalized version of equation 3.4 can be used to understand the (kinematic) similarities between source and receiver wavefields. This concept is known as extended imaging (Rickett and Sava, 2002; Sava and Fomel, 2006; Sava and Vasconcelos, 2011). A general

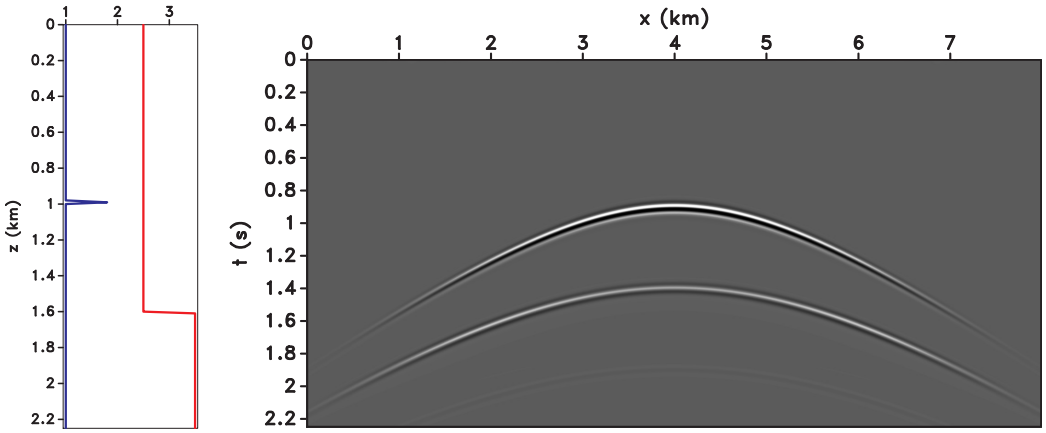


Figure 3.1: Synthetic experiment setup: (a) the density (spike function) model (g/cc) and the velocity (step function) model (km/s), and (b) the modeled data.

case of an extended image is defined as follows:

$$R(\mathbf{x}, \boldsymbol{\lambda}, \tau) = \sum_e \sum_t u_s(e, \mathbf{x} - \boldsymbol{\lambda}, t - \tau) u_r(e, \mathbf{x} + \boldsymbol{\lambda}, t + \tau), \tag{3.6}$$

where $\boldsymbol{\lambda}$ and τ are space and time extensions of the cross-correlation, respectively. Extended images are commonly used to produce angle gathers (Sava and Fomel, 2006; Sava and Vlad, 2011; Sava and Fomel, 2003) and for velocity estimation (Shen and Symes, 2008; Yang and Sava, 2011b; Yang et al., 2013).

In the presence of sharp models, we can substitute equations 3.2 and 3.3 into equation 3.6. By doing so, we can differentiate between the different components of the extended image, which is similar to what we do for conventional images:

$$\begin{aligned} R(\mathbf{x}, \boldsymbol{\lambda}, \tau) = R^{ff}(\mathbf{x}, \boldsymbol{\lambda}, \tau) + R^{bb}(\mathbf{x}, \boldsymbol{\lambda}, \tau) \\ + R^{bf}(\mathbf{x}, \boldsymbol{\lambda}, \tau) + R^{fb}(\mathbf{x}, \boldsymbol{\lambda}, \tau). \end{aligned} \tag{3.7}$$

The reflected data maps into the components ^{ff} and ^{bb}, whereas the backscattered energy maps into the ^{fb} and ^{bf} components.

In the conventional image $R(\mathbf{x})$ (both backscattered and reflected energy) coexist above sharp interfaces, for example due to the presence of a salt body. The two components are

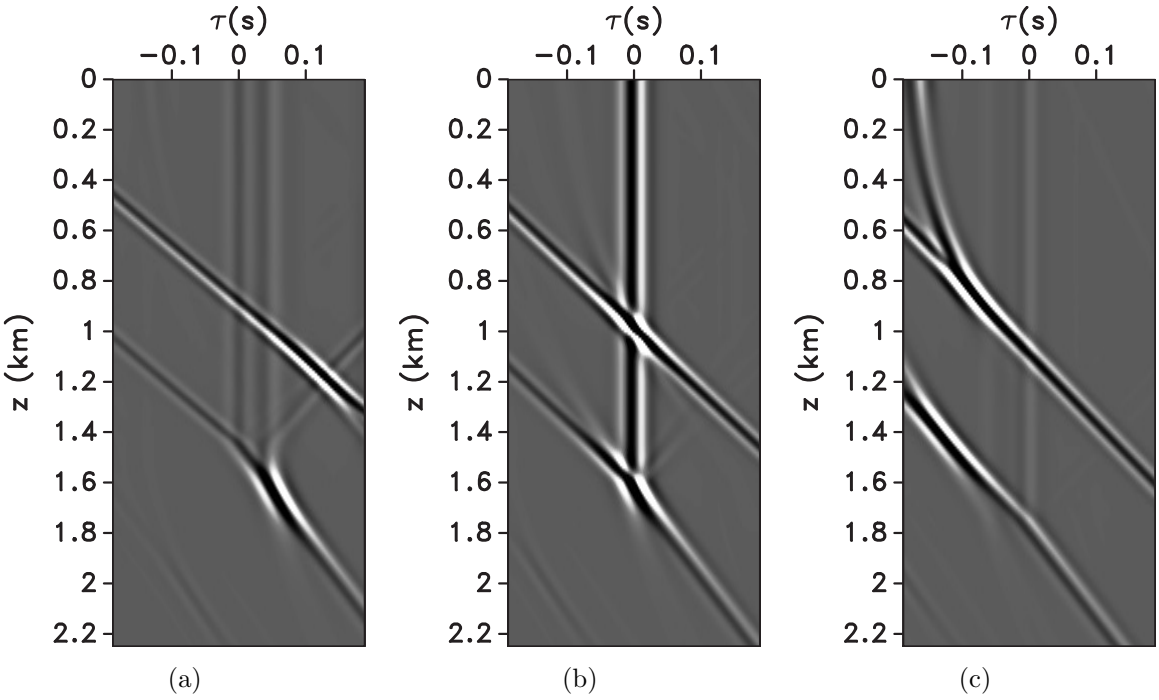


Figure 3.2: Time-lag gathers for (a) low, (b) correct and (c) high velocities.

usually separated based on the spectral content (the artifacts have low wavenumber content, whereas the reflectivity has high wavenumber content). This separation is normally done using some sort of high-pass filter, like a Laplacian (∇^2) operator (Youn and Zhou, 2001; Zhang and Sum, 2009) or by least-squares filtering (Guitton et al., 2007). The separation is not perfect in areas with similar spectral content. In the extended image space, however, the reflected and backscattered energy have unique mapping patterns (Díaz and Sava, 2012), which can be used to effectively separate both components (Kaelin and Carvajal, 2011). Díaz and Sava (2012) show that the backscattered and reflected energy share the wavefield synchronization criterion. The spatial and temporal synchronization occurs above a sharp boundary for backscattered events, whereas the synchronization occurs at the position of the reflectors for reflected data. The synthetic model shown in Figure 3.1(a) illustrates the extended image kinematic sensitivity to model error. The data in Figure 3.1(b) show two events: the earlier one corresponding to a reflector in the density model (spike in Fig-

ure 3.1(a)), and the later one resulting from a sharp contrast in the velocity model (step function in Figure 3.1(a)). The third event in the data corresponds to an internal multiple generated between the density and velocity interfaces.

Figures 3.2(a), 3.2(b), and 3.2(c) show time-lag gathers for three different velocities. These gathers are generated using equation 3.6 with $\boldsymbol{\lambda} = \mathbf{0}$ after stacking over different experiments, i.e. shots in this case. We simulate a velocity error in the first layer and adjust the sharp boundary according to the migration velocity, for example a low velocity shifts the boundary upwards and a high velocity shifts the boundary downwards. The backscattering maps vertically in the three cases, however it deviates from $\tau = 0$ when the velocity is incorrect. The time delay error in the backscattering is the same to the one produced by the reflected energy at the sharp interface. Therefore, the backscattering provides information about the sharp interface at any place in the image above it.

Figures 3.3(a), 3.3(b), and 3.3(c) show the equivalent space-lag gather dependency with respect to the velocity error. Similar to the time-lag gathers, the space-lag gathers are generated after stacking the contribution from different experiments. The backscattering (mapping vertically in the gathers) spreads away from $\lambda_x = \mathbf{0}$ with the velocity error, thus emulating the defocusing of the reflected data. Similarly to the time-lag gathers, the backscattering above the interface is the expression of the defocusing at the sharp boundary.

Since both reflected and backscattered data share similar velocity dependency, we conclude that we can design an inverse problem that optimizes both type of events simultaneously (Díaz and Sava, 2012). The following subsection details the velocity analysis procedure based on backscattering.

3.3 Wavefield tomography with extended images

In order to analyze the velocity model error, we can make use of the semblance principle which seeks image consistency as a function of extended image parameters. Stork (1992) implements the idea using the consistency between common offset images. Symes and Carazzone (1991) exploit this concept using the differential semblance optimization (DSO) method.

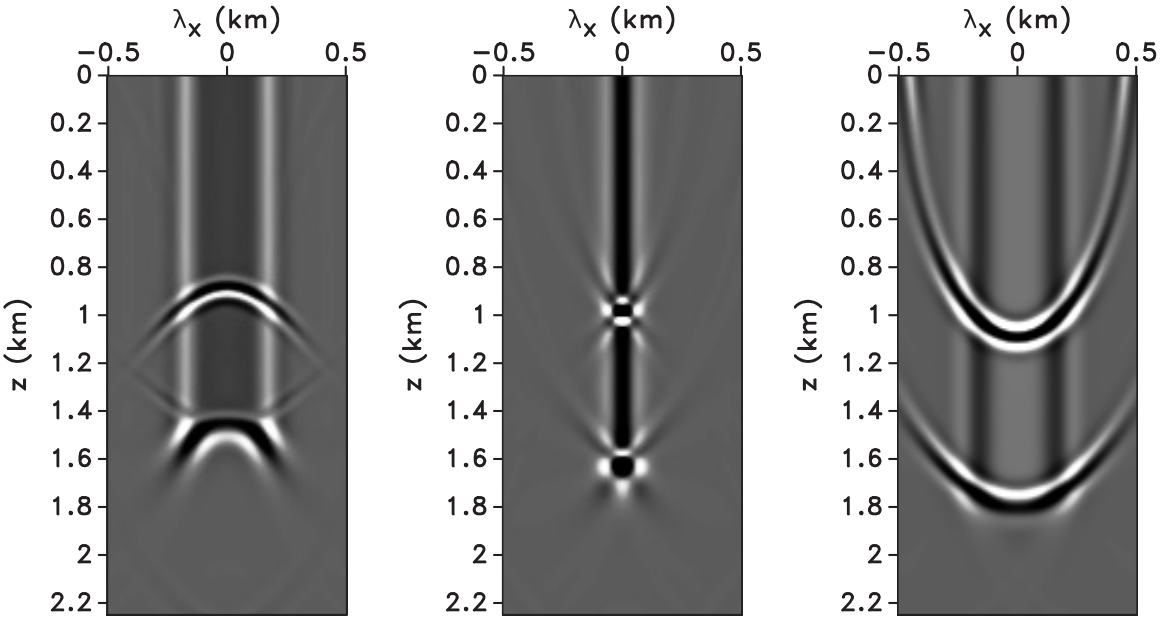


Figure 3.3: Space-lag gathers for (a) low, (b) correct and (c) high velocities.

DSO can also be used to increase the flatness of angle gathers. Rickett and Sava (2002) and Sava and Fomel (2003) show that common angle gathers and extended images are related by a slant stacking operation. Therefore, these two type of common image gathers are equivalent for velocity analysis. Shen and Symes (2008) and Yang and Sava (2011a) use the consistency criterion in extended images to formulate a tomographic problem based on space-lag gathers or joint space and time-lag gathers, respectively.

3.3.1 Inversion with time-lag gathers

If the velocity is correct, the time-lag gathers (Sava and Fomel, 2006) show maximum focusing at zero lag. This observation derives from the fact that the source and receiver wavefields are synchronized at the reflector position. The velocity model can be improved by increasing the wavefield synchronization, which is equivalent to locating the events in the extended images as close as possible to $\tau = 0$. This can be done by minimizing the following

objective function (OF):

$$J = \frac{1}{2} \left|\left| P(\tau) R(\mathbf{x}, \tau) \right|\right|^2 , \tag{3.8}$$

where $P(\tau) = |\tau|$ is an operator that penalizes the energy outside $\tau = 0$. Following the notation in Yang and Sava (2011a), we can express $R(\mathbf{x}, \tau)$ as

$$R(\mathbf{x}, \tau) = \sum_e \sum_t T(-\tau) u_s(e, \mathbf{x}, t) T(+\tau) u_r(e, \mathbf{x}, t), \tag{3.9}$$

where $T(\pm\tau)$ is a time-shift operator applied to the source or receiver wavefields. Note that this OF cannot drop to zero completely because in the time-lag gathers, the wavefields correlate for all values of τ. Here we are interested in bringing the maximum of the correlation towards $\tau = 0$. However, this OF is minimum when the velocity model is correct and most of the energy in the extended image locates at $\tau = 0$.

We compute the gradient of equation 3.8 using the Adjoint State Method (ASM) (Plessix, 2006; Tarantola, 1984). The adjoint source with respect to the source wavefield for an experiment e is

$$g_s(\mathbf{x}, e) = \sum_\tau T(-\tau) P^2(\tau) R(\mathbf{x}, \tau) T(-\tau) u_r(e, \mathbf{x}, t), \tag{3.10}$$

and the adjoint source with respect to the receiver wavefield is

$$g_r(\mathbf{x}, e) = \sum_\tau T(\tau) P^2(\tau) R(\mathbf{x}, \tau) T(\tau) u_s(e, \mathbf{x}, t). \tag{3.11}$$

We construct the adjoint state variables by injecting the adjoint sources at the gather positions and by extrapolating the wavefields using the adjoint modeling operators. The adjoint source wavefield $a_s(e, \mathbf{x}, t)$ is reconstructed backward in time, whereas the adjoint receiver wavefield $a_r(e, \mathbf{x}, t)$ is reconstructed forward in time. Using the state and adjoint state variables, the gradient with respect to the velocity model is

$$\nabla J(\mathbf{x}) = \frac{-2}{v^3(\mathbf{x})} \sum_e \sum_t \frac{\partial^2 u_s}{\partial t^2}(e, \mathbf{x}, t) a_s(e, \mathbf{x}, t) + \frac{\partial^2 u_r}{\partial t^2}(e, \mathbf{x}, t) a_r(e, \mathbf{x}, t), \tag{3.12}$$

where $\frac{-2}{v^3(\mathbf{x})}\frac{\partial^2}{\partial t^2}$ corresponds to the derivative of the modeling operator (equation 3.1) with respect to the velocity model.

In the gradient expression (equation 3.12) we expect to correlate state and adjoint state wavefields traveling in the same direction which implies that the gradient is smooth. However, if backscattering is present in the wavefield, we obtain cross-talk producing reflectors in the gradients. The cross-talk in this case is generated by the correlation of wavefields traveling in the opposite direction. In order to attenuate the cross-talk, we can use a filter that preserves the components of wavefields traveling in the same direction and eliminates the wavefields traveling in opposite directions. We can find the direction of propagation using the approach of Yoon et al. (2004), which constructs the Poynting vectors $\mathbf{P}(e, \mathbf{x}, t)$ using the equation

$$\mathbf{P}(e, \mathbf{x}, t) \propto \frac{\partial u(e, \mathbf{x}, t)}{\partial t} \nabla u(e, \mathbf{x}, t), \tag{3.13}$$

where u can be either the source or the receiver wavefield. In practice we use the time-averaged Poynting vectors using a Gaussian smoothing over a small time window determined by the dominant period of the data

$$< \mathbf{P}(e, \mathbf{x}, t) >_t = \mathbf{P}(e, \mathbf{x}, t) * G(t). \tag{3.14}$$

Here, the symbol $*$ denotes convolution, and $G(t)$ is the Gaussian smoothing filter. The smoothed Poyting vector contains the propagation information of the most energetic arrival in the wavefields, which mishandle cases like multipathing.

To keep just the wavefields components traveling in the same direction, we can compute a weighting function $W(\theta)$ with

$$\theta(\mathbf{x}, t) = \cos^{-1}\left(\frac{\mathbf{P}_s(\mathbf{x}, t) \cdot \mathbf{P}_r(\mathbf{x}, t)}{|\mathbf{P}_s(\mathbf{x}, t)||\mathbf{P}_r(\mathbf{x}, t)|}\right) \tag{3.15}$$

such that we preserve the wavefield cross-correlation for which $\mathbf{P}_s(\mathbf{x}, t) \cdot \mathbf{P}_r(\mathbf{x}, t) \approx 1$, i.e. when the direction of propagation is similar within a given tolerance. The weighting function can be designed using a cutoff angle, from which the function tapers off smoothly using a Gaussian function with standard deviation σ which defines the range from which the angles

are accepted.

$$W(\theta, a, \sigma) = \begin{cases} 1 & \text{if } 0^\circ \leq \theta < a; \\ e^{-(\theta-a)^2/(2\sigma^2)} & \text{if } a \leq \theta \leq 180^\circ. \end{cases} \tag{3.16}$$

Based on this filter, we change equation 3.12 to

$$\nabla J(\mathbf{x}) = \frac{-2}{v^3(\mathbf{x})} \sum_e \sum_t W(\theta) \frac{\partial^2 u_s}{\partial t^2}(e, \mathbf{x}, t) a_s(e, \mathbf{x}, t) + W(\theta) \frac{\partial^2 u_r}{\partial t^2}(e, \mathbf{x}, t) a_r(e, \mathbf{x}, t). \tag{3.17}$$

This new gradient avoids cross-talk and emphasizes wavefields traveling in the same direction. This method increases the cost of the correlation step. If the smoothing stencil along time axis is short, then efficient options like check-point access could be used for propagating wavefields and computing the propagation directions (Symes, 2007).

Figures 3.4(a), 3.4(c), and 3.4(e) show the gradient constructed using equation 3.12 for low, correct, and high velocities, respectively. One can see that the intensity of the gradient with correct velocity is lower than the obtained for either low or high velocities. One can also observe the cross-talk due to wavefields propagating in opposite directions which appears in the gradient similarly to reflectors present in a migrated image. The gradient is computed using equation 3.17 with a cutoff angle $a = 15^\circ$. Figures 3.4(b), 3.4(d), and 3.4(f) show the cross-talk significantly attenuated.

3.3.2 Inversion with space-lag gathers

We can also use the information contained in space-lag gathers (Rickett and Sava, 2002). If the velocity model is correct, then space-lag gathers focus at $(\lambda_x, \lambda_y) = (0, 0)$. If the velocity model is incorrect, the gathers contain defocused energy outside $\boldsymbol{\lambda} = \mathbf{0}$. This criterion is used by Shen and Symes (2008); Weibull and Arntsen (2013); Yang and Sava (2011a) to formulate wavefield tomography using the OF

$$J = \frac{1}{2} \left|\left| P(\boldsymbol{\lambda}) R(\mathbf{x}, \boldsymbol{\lambda}) \right|\right|^2, \tag{3.18}$$

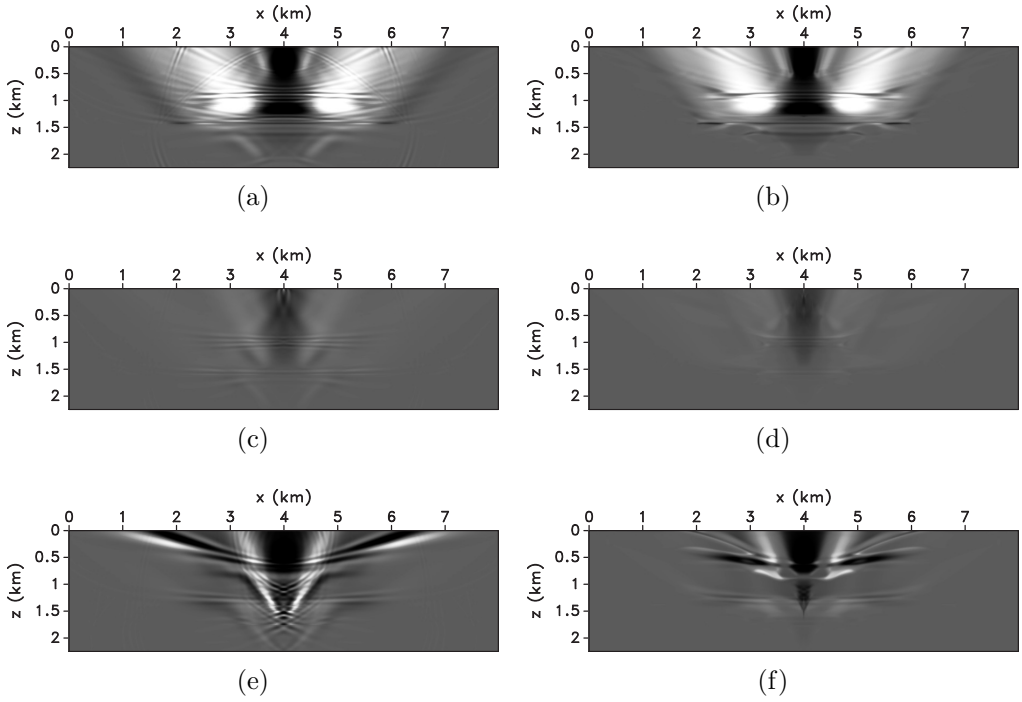


Figure 3.4: Gradients obtained using time-lag gathers for (a)-(b) low, (c)-(d) correct, and (e)-(f) high velocities. Gradients (a), (c), and (e) are constructed without filtering and (b), (d) and (f) with filtering.

where $P(\boldsymbol{\lambda}) = |\boldsymbol{\lambda}|$ is a penalty operator. Even with correct velocity, this OF does not become zero due to the band-limited nature of the data and due to illumination effects (Yang et al., 2013). Nevertheless, this OF provides an effective criterion for velocity updating.

We compute the gradient of equation 3.18 using the same workflow as the one used for equation 3.8 (Yang and Sava, 2011a). The adjoint sources are defined as

$$g_s(\mathbf{x}, e) = \sum_{\boldsymbol{\lambda}} T(-\boldsymbol{\lambda}) P^2(\boldsymbol{\lambda}) R(\mathbf{x}, \boldsymbol{\lambda}) T(-\boldsymbol{\lambda}) u_r(e, \mathbf{x}, t) \tag{3.19}$$

for the source side, and

$$g_r(\mathbf{x}, e) = \sum_{\boldsymbol{\lambda}} T(+\boldsymbol{\lambda}) P^2(\boldsymbol{\lambda}) R(\mathbf{x}, \boldsymbol{\lambda}) T(+\boldsymbol{\lambda}) u_s(e, \mathbf{x}, t) \tag{3.20}$$

for the receiver side. Here $T(\pm\boldsymbol{\lambda})$ is a space shifting operator applied to the wavefields. The only difference between the time-lag and space-lag gather formulation is in the OF and in the computation of the adjoint sources. The gradient and adjoint wavefields are computed using the same wave-equation and background velocity model as in the case of the time-lag gathers (equations 3.12 and 3.17).

Figures 3.5(a), 3.5(c), and 3.5(e) show the gradients for low, correct, and high velocity, respectively. To compute these gradients, we use the space-lag gathers depicted in Figures 3.3(a), 3.3(b), and 3.3(c), respectively. As for the gradient constructed with time-lag gather, one can see that the energy in the space-lag gradient is proportional to the focusing error observed in the gathers. The gradients obtained using equation 3.12 also contain cross-talk similarly to the gradient constructed with time-lag gathers. If we apply the directional filtering during the gradient computation (equation 3.17), we obtain gradients with significantly lower cross-talk. Figures 3.5(b), 3.5(d), and 3.5(f) show the filtered gradients for the low, correct, and high velocity models, respectively.

3.4 Examples

In this section, we illustrate how to use the backscattering and reflected events with two examples: one with a simple setting including a Gaussian anomaly and the second with a truncated version of the Sigsbee model around the sediment basin. With the first example,

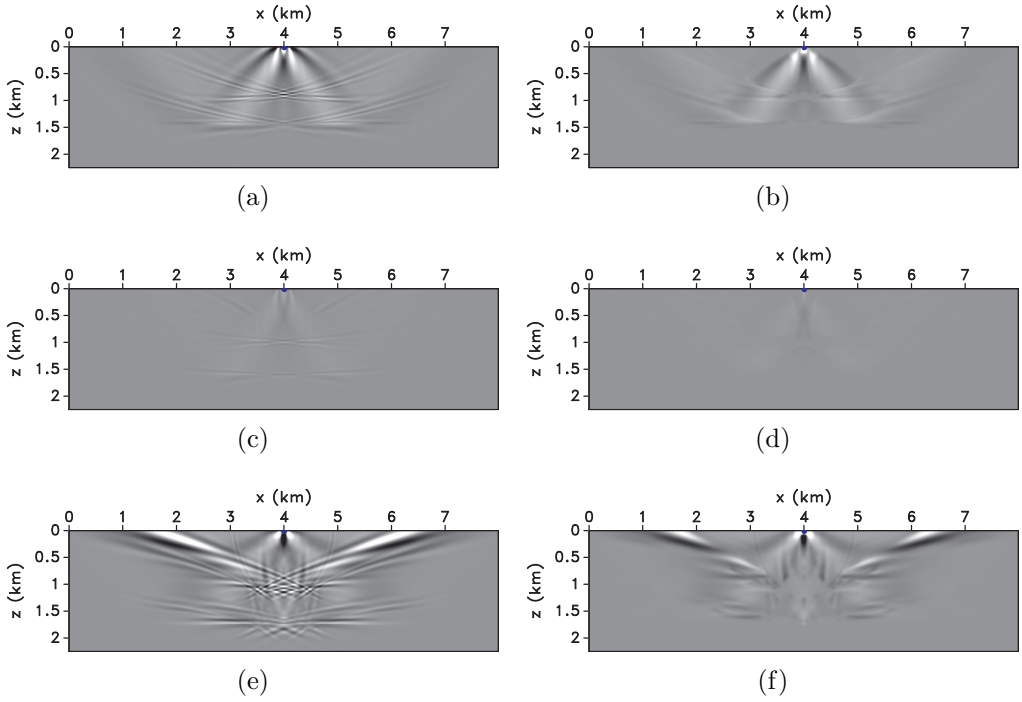


Figure 3.5: Gradients obtained using space-lag gathers for (a)-(b) low, (c)-(d) correct, and (e)-(f) high velocities. Gradients (a), (c), and (e) are constructed without filtering and (b), (d) and (f) with filtering.

we introduce the methodology for iterative boundary update, and with the second, we show its application to a more realistic example.

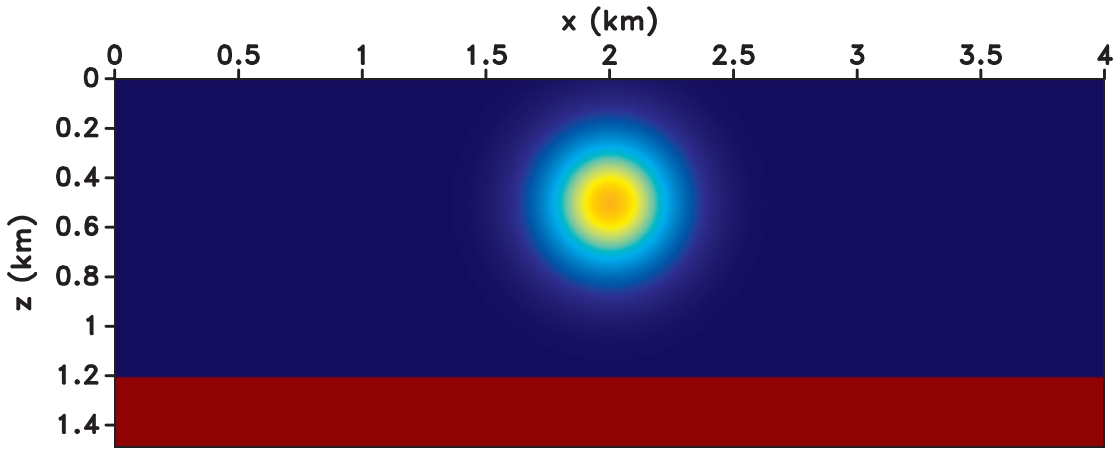
3.4.1 Simple model with a Gaussian anomaly

In this example we test a model with a Gaussian anomaly where we can better predict the location of the sharp boundary at each iteration. The model consists of a homogeneous background model of 2km/s with a positive Gaussian anomaly of +15% relative to the background, shown in Figure 3.6(a). We create data with a surface receiver array and 41 sources evenly distributed. We perform two inversion tests, the first with the conventional approach (no sharp boundary), using the starting model shown in Figure 3.6(b), and the second test using the starting model depicted in Figure 3.6(c). Figures 3.7(a) and 3.8(a) show the images for the starting model without and with the sharp boundary, respectively.

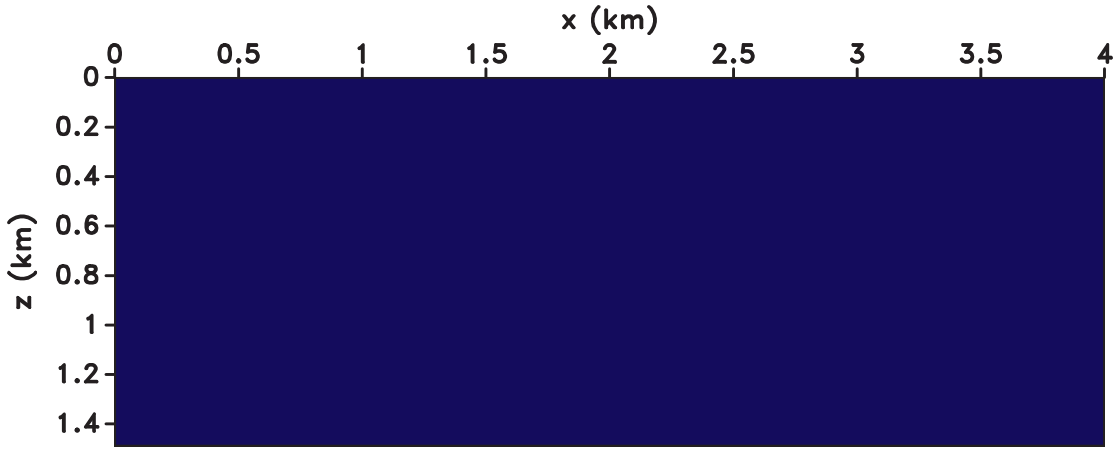
The initial space-lag gathers are shown in Figure 3.7(b) and Figure 3.8(b) for starting velocities without and with a sharp boundary, respectively. The gathers lag axis ranges from -0.4km to 0.4km. Note the backscattering in Figure 3.8(b), which highlights the defocusing of the deepest event everywhere above this event.

We perform these two inversions using a steepest descent solver with a parabolic line search. For each case, we use 10 iterations. After both inversions, the extended images have better focusing as shown in Figures 3.9(b) and 3.10(b). Figures 3.9(a) and 3.10(a) show the final images for both inversions. The inversion using the backscattering shows improvement in the flatness of the second and third layer, because it promotes better focusing in the lower part of the model. Without backscattering, the focusing measured in the second layer is only sensitive to the velocity above this layer, whereas with backscattering we can pick up focusing information from the deepest layers. Adding the sharp boundary is equivalent to putting more weight on the focusing error of the deepest reflector.

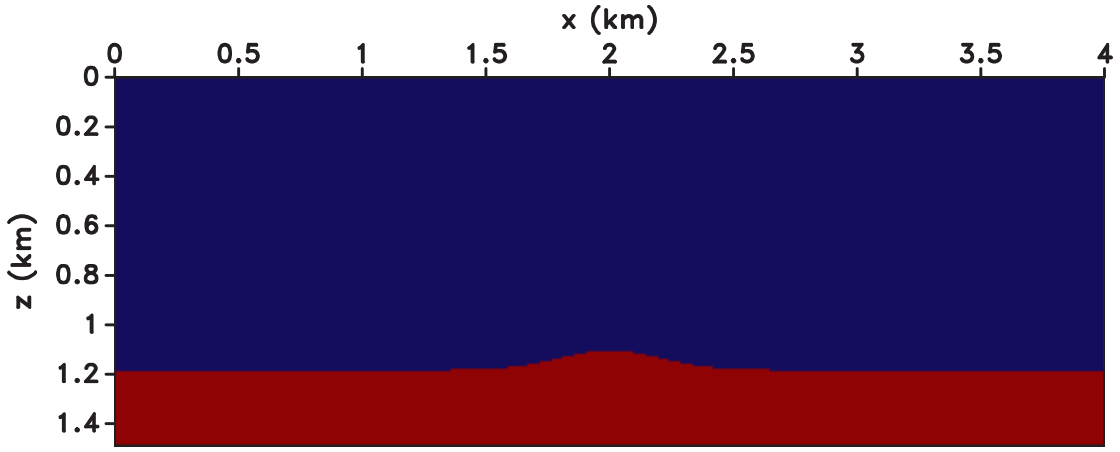
As mentioned in the previous section, tomography with backscattering requires iterative update of both the velocity model and the sharp boundary. For this particular inversion problem, we iteratively update the boundary position from depth to time using the velocity



(a)

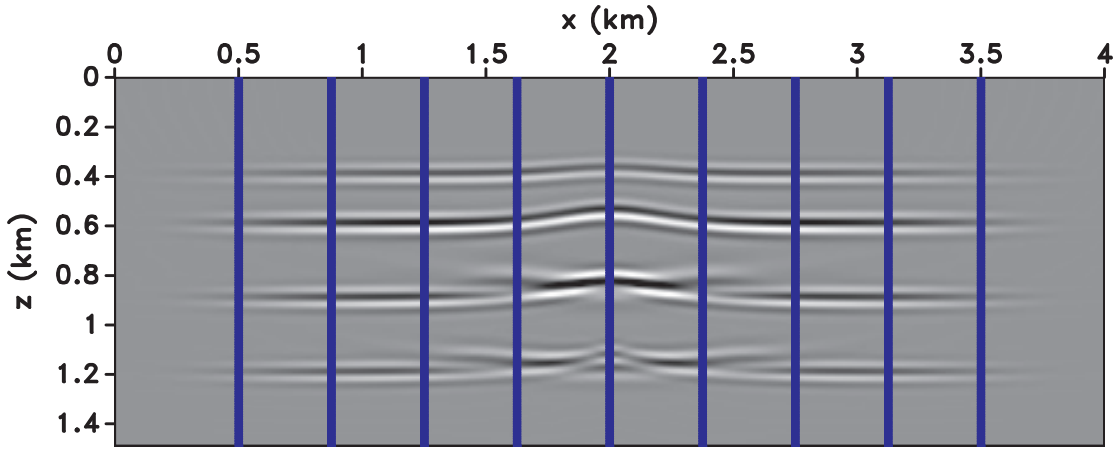


(b)

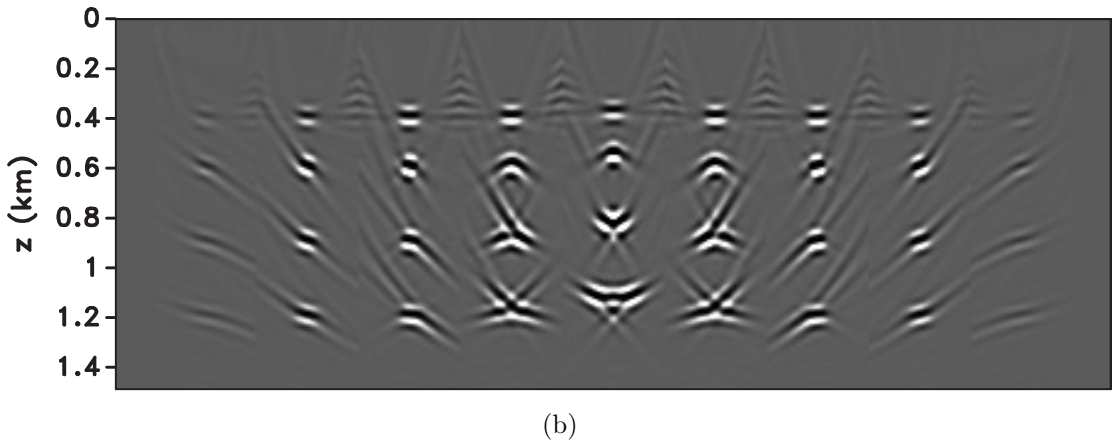


(c)

Figure 3.6: (a) Gaussian velocity model, (b) starting velocity without the sharp boundary and (c) starting model with the sharp boundary.

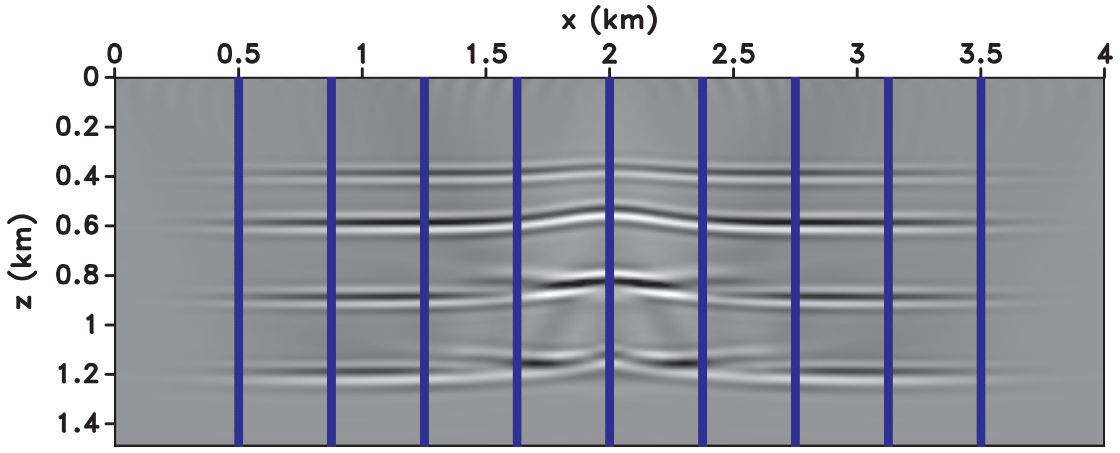


(a)

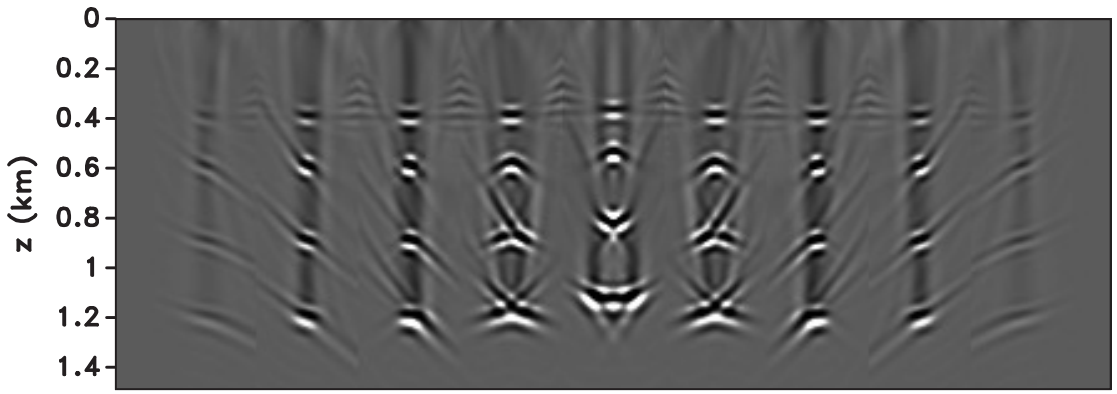


(b)

Figure 3.7: (a) Conventional image from starting model in 3.6(b), and (b) its space-lag gathers. Note the structural anomaly in the middle of the image (top). Compare with Figure 3.9(a). The blue lines show the location of the gathers.

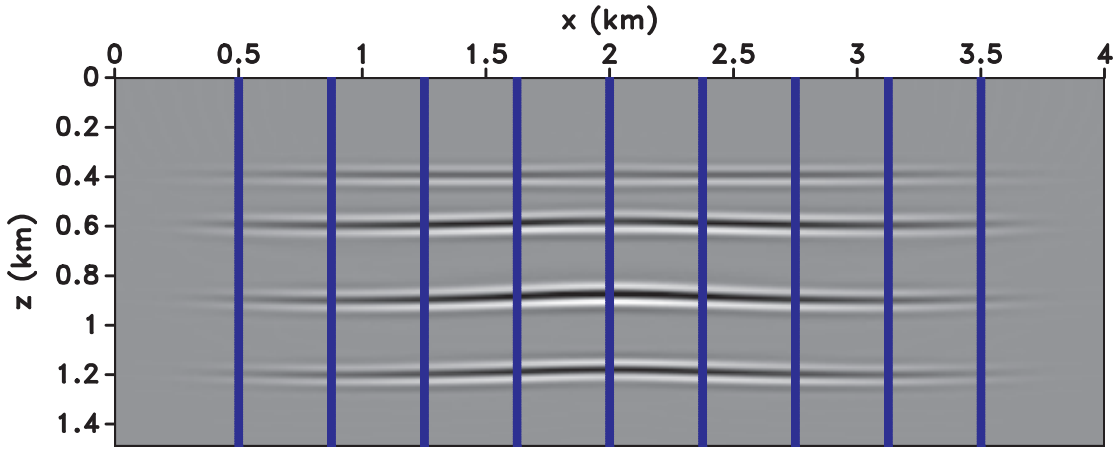


(a)

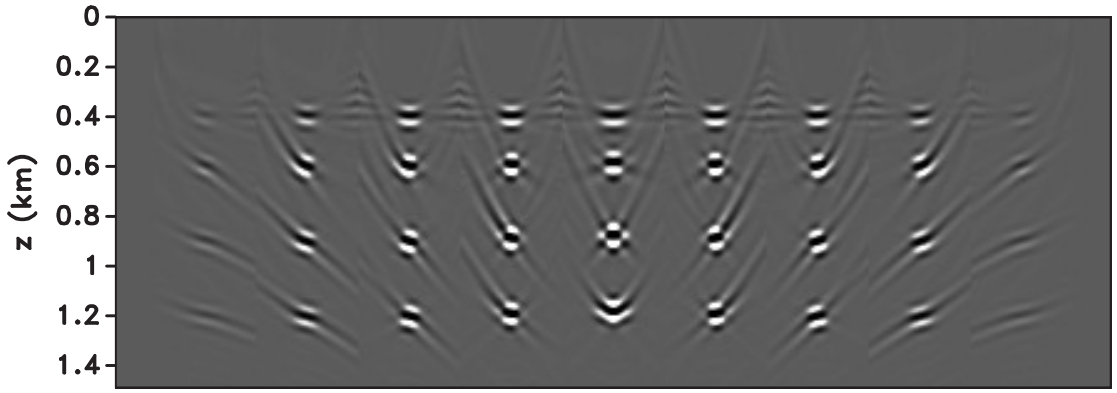


(b)

Figure 3.8: (a) Conventional image from starting model in 3.6(c), and (b) and its space-lag gathers. Note how the backscattering spreads the defocusing of the events in the conventional image (top). Compare with optimized image in Figure 3.10(b).

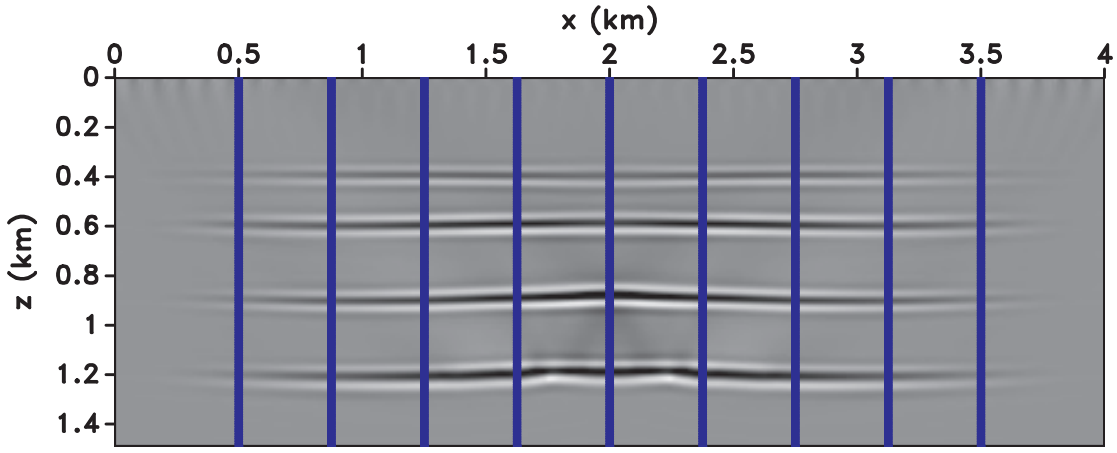


(a)

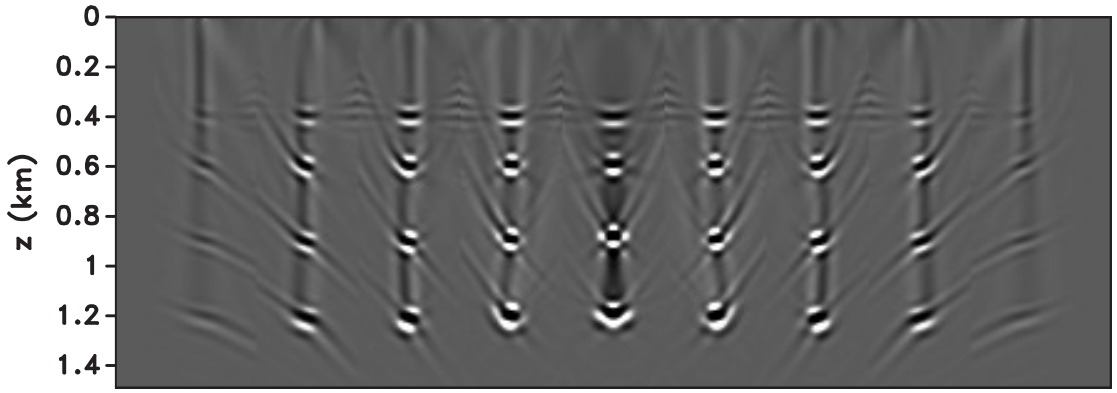


(b)

Figure 3.9: (a) Conventional image from inverted model without the sharp boundary, and (b) its space-lag gathers.

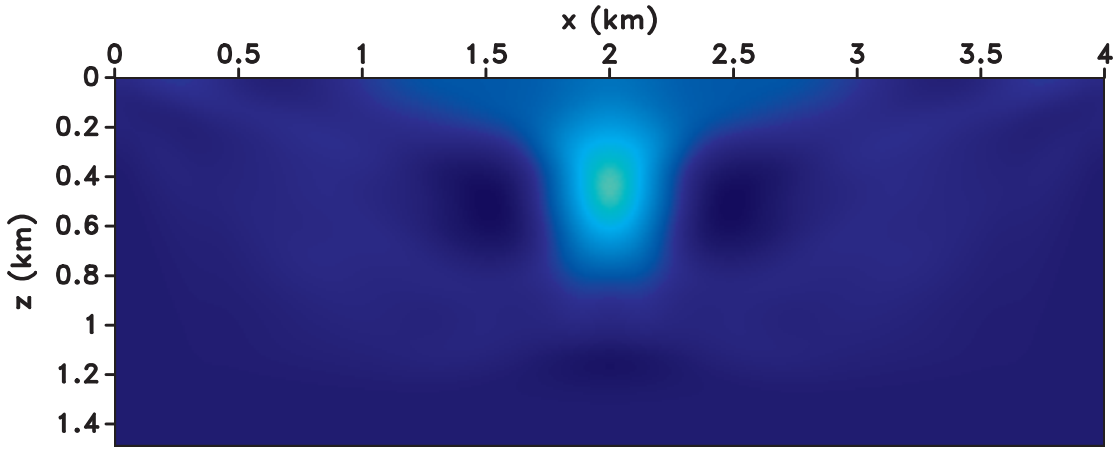


(a)

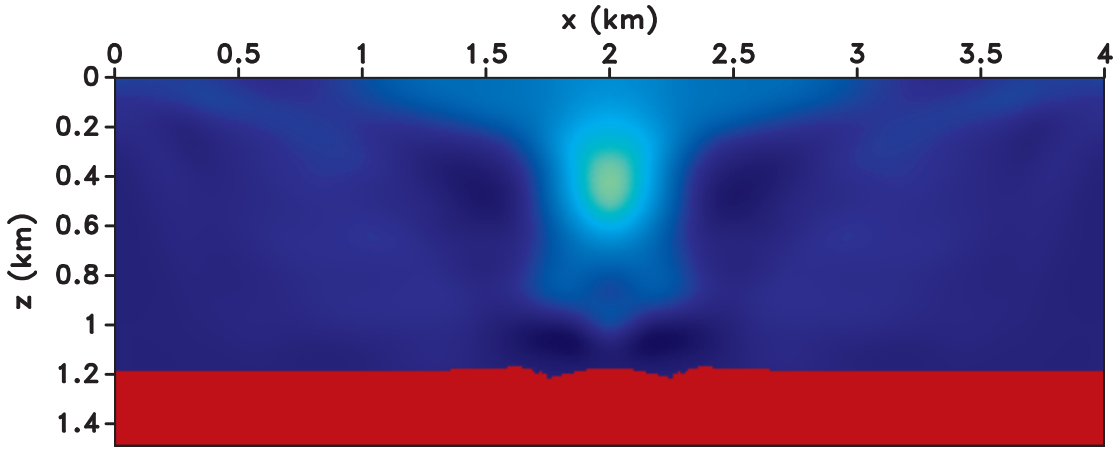


(b)

Figure 3.10: (a) Conventional image from inverted model with the sharp boundary, and (b) its space-lag gathers.



(a)



(b)

Figure 3.11: (a) Final inverted velocity models without the sharp boundary, and (b) with the sharp boundary.

$V^{it}(\mathbf{x})$ and stretching back to depth using the velocity $V^{it+1}(\mathbf{x})$, where the superscript relates to the iteration number. This scheme implicitly assumes that the vertical traveltime is preserved. For stretching to time we use

$$t_i = t_{i-1} + \frac{z_i^{it} - z_{i-1}^{it}}{V^{it}(z_i)}, \tag{3.21}$$

with $t_0 = 0$, and for stretching back to depth we use

$$z_i^{it+1} = z_{i-1}^{it+1} + V^{it+1}(z_i)(t_i - t_{i-1}). \tag{3.22}$$

This vertical stretching assumes that the traveltime is affected only by the velocity above the sharp boundary, so it would be naive to use it under strong lateral velocity variations as explained in Cameron et al. (2008). Nevertheless, this approach works for this example and it helps us illustrate the strengths of the methodology. To help to correct accumulated prediction errors during the iterative process, one could repick the boundary after some iterations or allow an alternative automatic process to move a known interface based on an updated image.

Finally, Figures 3.11(a) and 3.11(b) show the inverted models without the sharp boundary and with the sharp boundary strategy, respectively. We can observe that the inverted model with the sharp boundary has fewer side lobes around the recovered anomaly and higher velocity at the anomaly. Despite the fact that the recovered anomaly for the sharp boundary better focus the events, the geometry of the sharp boundary is not flat. The inaccurate boundary prediction is due to the lateral homogeneous assumption for predicting the sharp boundary.

3.4.2 Complex model based on the Sigsbee 2A velocity

Here, we illustrate the use of the backscattering and reflected events on a small portion of the Sigsbee 2b model (Paffenholz et al., 2002). We focus on the small basin formed by the salt intrusion (Figure 3.12(a)) due to its structural complexity and because it generates considerable backscattering energy. We simulate data for 61 shots evenly distributed on

the surface, with a fixed receiver array at the surface. Figure 3.12(b) shows the migrated data using the correct velocity model, and Figure 3.12(c) shows the corresponding space-lag gathers. The λ_x axis goes from -0.4km to +0.4km for all cases in this section.

Similar to our work with the previous example, we perform two inversion tests: one with the conventional strategy and one with the new method. We test the method using a slow sediment velocity with an error increasing with depth, as shown in Figure 3.13(a). Figure 3.13(b) depicts the RTM image for this model, and Figure 3.13(c) shows the corresponding space-lag gathers. We interpret a salt boundary from the RTM image with slow sediment velocity, and add the salt layer to the model as shown in Figure 3.14(a). Note how the incorrect velocity model, along with the inaccurate boundary, produces strong artifacts in the image. These artifacts are produced because the $R^{ff}(\mathbf{x})$ and $R^{bb}(\mathbf{x})$ components of the image do not map to the same position for incorrect velocity. Figures 3.14(b) and 3.14(c) show the RTM image and the respective space-lag gathers for the starting velocity with the sharp boundary. Note how the backscattering in Figure 3.14(c) spreads away from zero lag. It is worth noticing how the backscattering in the RTM image (Figure 3.14(b)) varies throughout the section and produces two events originating in the deepest part of the basin.

The inversion without backscattering has difficulties updating the model inside the basin, and produces an anomaly near the water bottom as depicted in Figure 3.15(a). This velocity produces incorrect reflector depths, as shown by the image in Figure 3.15(b); however, the corresponding space-lag gathers, Figure 3.15(c), show good focusing.

Figure 3.16(a) shows the final inverted model using the new method; note how the velocity inside the basin is better retrieved than in the conventional approach. Figures 3.16(b) and 3.16(c) show the final RTM image and the corresponding gathers, respectively. Note how the inverted model correctly focuses all the energy to zero lag. Also, the final gathers have simpler characteristics (without crossing events) compared to those of Figure 3.14(b). The backscattering even is consistent throughout the section. This consistency of the backscattering can also be seen in the final RTM image, Figure 3.16(b). For updating the boundary

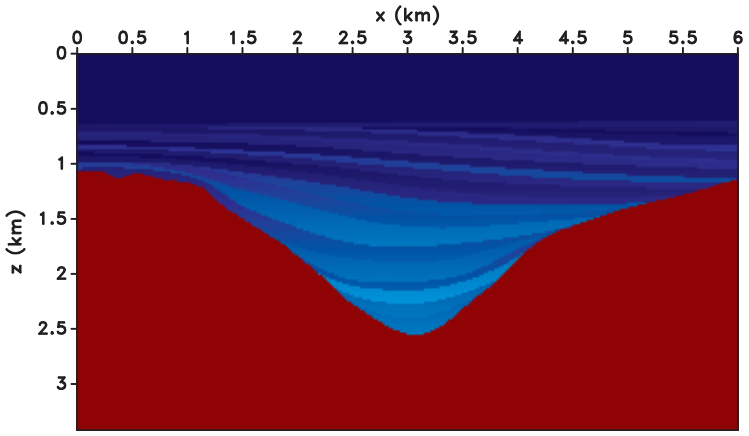
we use the same strategy as in the previous example. Despite not being consistent with the lateral homogeneous assumption, the TOS event moves down in the right direction as the velocity in the sediments increases.

3.5 Conclusions

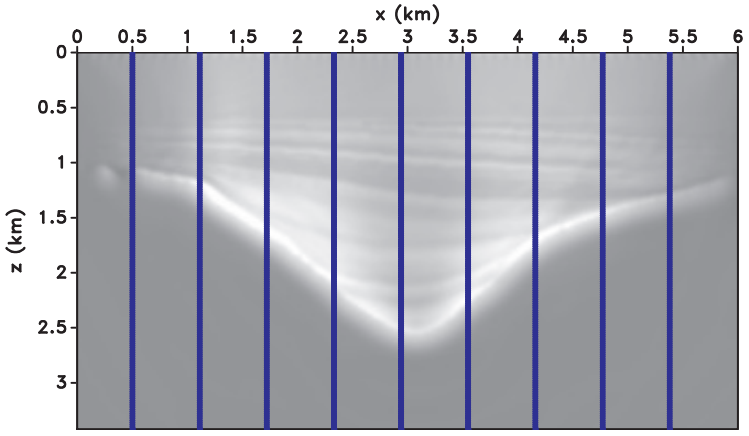
We demonstrate that RTM backscattering contains kinematic and focusing information that can be used for wavefield tomography. In order to include the backscattering in the tomography, we need sharp boundaries in the model. During the tomographic iterations both the velocity model and the sharp boundaries need to be updated. The sharp boundaries generate waves traveling in all directions for both state and adjoint state wavefields. Therefore, the gradient contains smooth and sharp components produced by the correlation of waves traveling in similar and opposite directions, respectively. We employ a directional filter based on Poyting vectors to isolate the gradient components corresponding to the correlation of waves traveling in the same direction. Our numerical experiments indicate that the model is better retrieved when we include the boundary in the inversion due to the fact that backscattering spreads information observed at the sharp boundary everywhere in the medium, increasing the weight of the deepest events during the tomographic update. The setup proposed in this paper leads to increased focusing of reflected energy above the boundary while at the same time maximizes the backscattered energy.

3.6 Acknowledgments

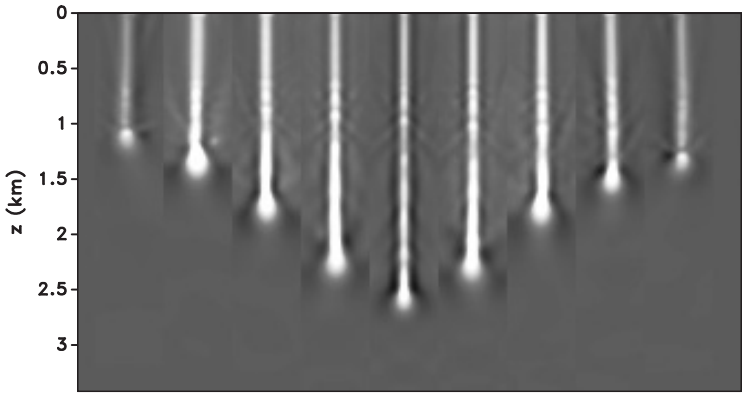
I would like to thank to Natalya Patrikeeva and Tongning Yang for stimulating discussions about the Poynting vector and wavefield tomography, respectively.



(a)

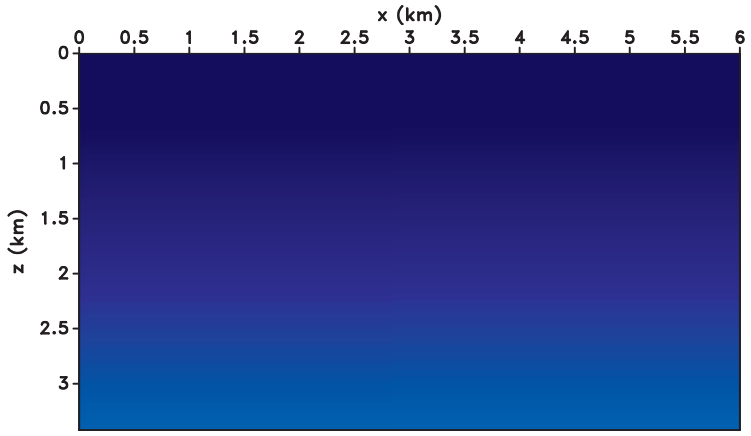


(b)

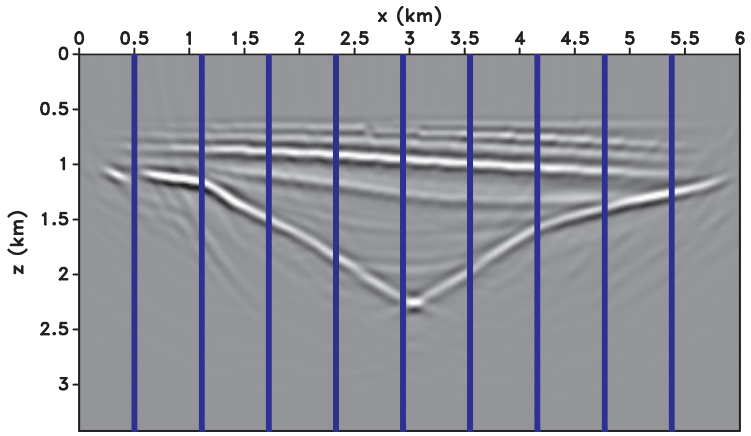


(c)

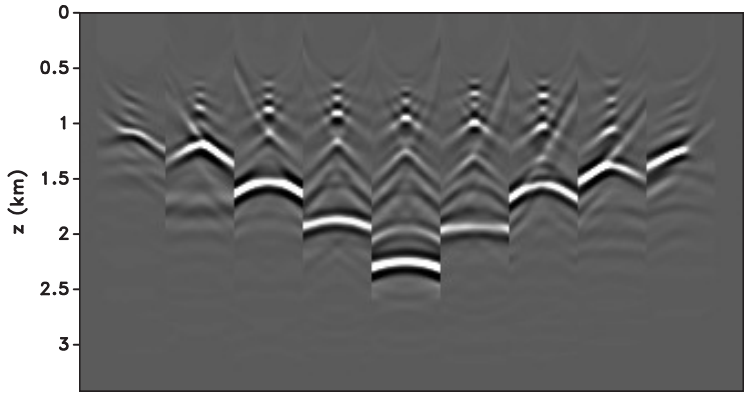
Figure 3.12: (a) True velocity model, (b) migrated data using true model and (c) space-lag.



(a)

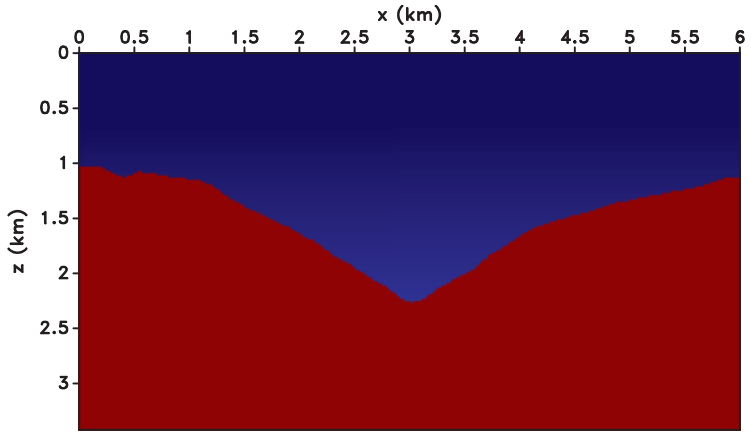


(b)

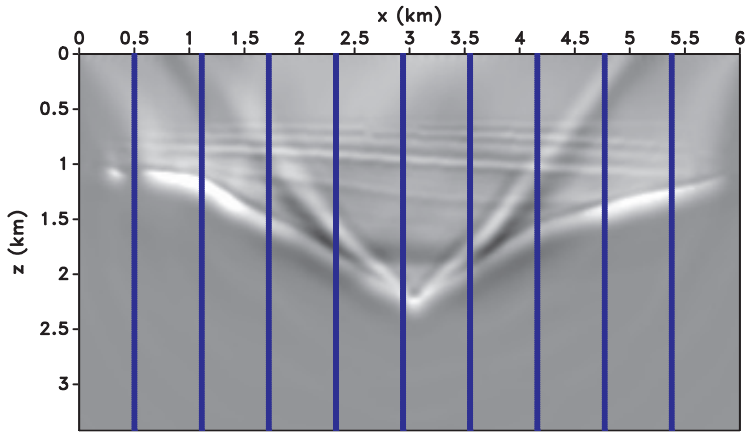


(c)

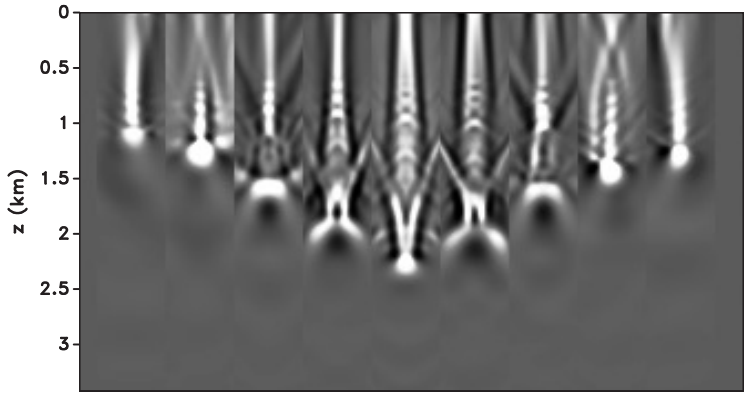
Figure 3.13: (a) Starting velocity model, (b) conventional image from starting model and (c) its space-lag gathers.



(a)

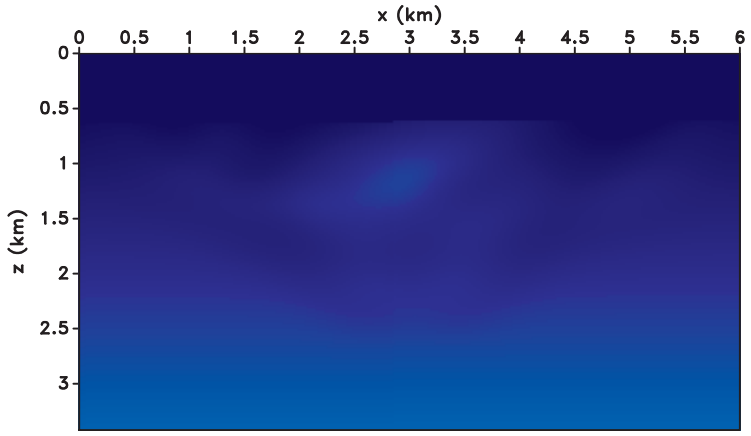


(b)

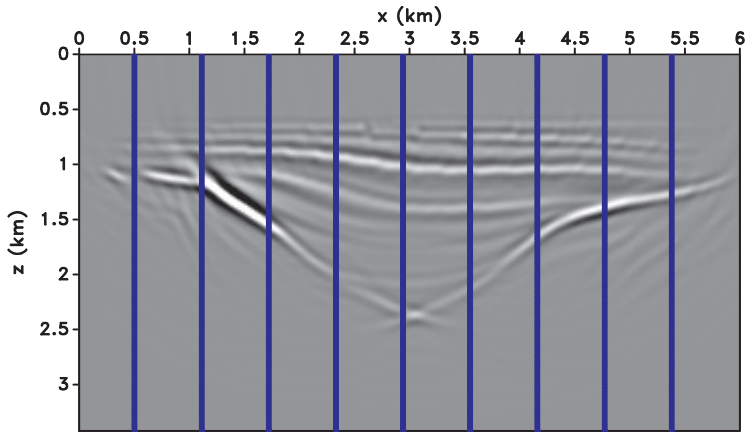


(c)

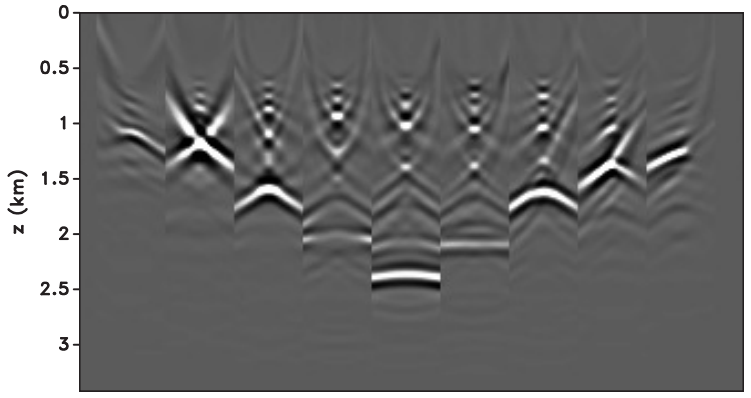
Figure 3.14: (a) Starting velocity model with sharp boundary, (b) corresponding migrated image, and (c) its space-lag gathers. Note the strong backscattering, and its spread from $\lambda_x = 0$.



(a)

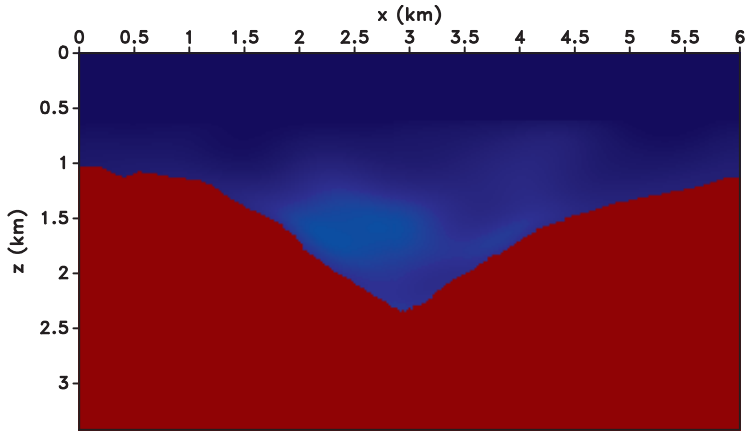


(b)

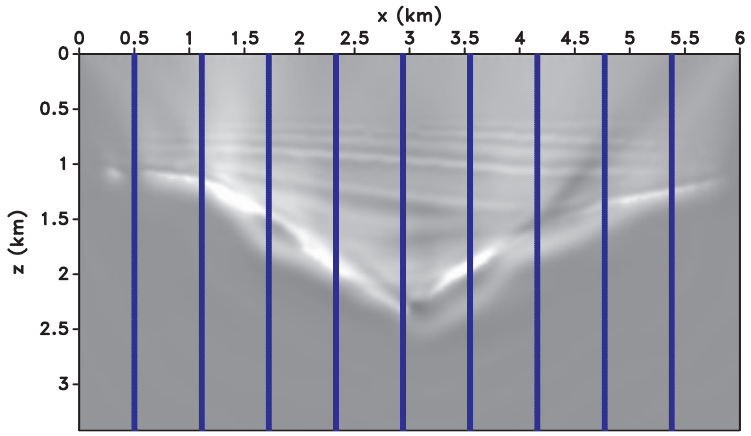


(c)

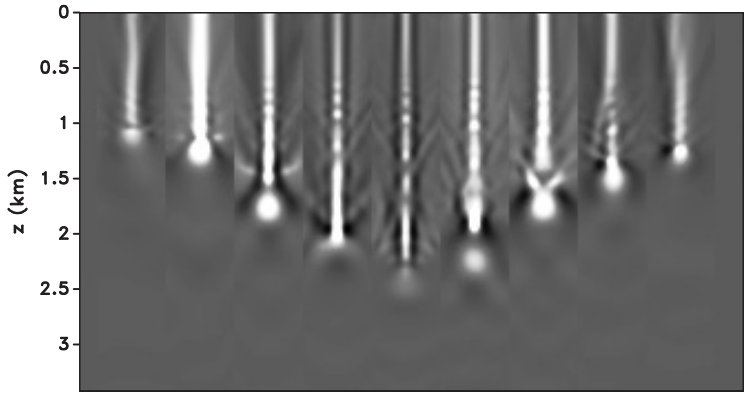
Figure 3.15: (a) Final inverted model for conventional approach, (b) final migrated image, and (c) the corresponding space-lag gathers.



(a)



(b)



(c)

Figure 3.16: (a) Final inverted model with sharp boundary, (b) final migration image and (c) its corresponding space-lag gathers. Note how the backscattering energy has been optimized and placed around $\lambda_x = 0$.

CHAPTER 4

CONCLUSIONS

In this thesis, I show that the so-called RTM artifacts contain kinematic and focusing information that can be used during migration velocity analysis. In the second chapter, I analyze such signatures in different flavors of extended images. Furthermore, I assert that the RTM backscattering can be used as a quantitative QC tool for the correct placement of the sediment-salt interface. This measure could be incorporated along with other image properties such as structure and coherency to estimate the salt boundary.

Ideally, we want to build a velocity model that honors the reflection data information above the sharp boundary and maximizes the RTM backscattering. For a lateral inhomogeneous model with a Gaussian anomaly, I show how to iteratively predict the sharp boundary and improve seismic focusing. I test the same workflow using a more complicated setting based on the Sigsbee model. The results show that the velocity anomalies are better recovered with the sharp boundary incorporated into the inversion. The backscattering adds focusing information from the deepest events in the basin, which gives more weight to this part of the residual in the inversion. In order to preserve the smoothness properties inherent in image domain inversion, one can add a Poynting vector filter that penalizes the correlation of wavefields traveling in opposite directions (the cross-talk). If the retrieved velocity model contains enough information in the low wavenumbers, one could continue the model recovery with alternative methods such as FWI to retrieve the rest of the model spectrum.

REFERENCES CITED

Ahmed, I., R. Faerber, C. Kumar, and F. Billette, 2012, Interactive velocity model validation (IVMV): SEG Technical Program Expanded Abstracts 2012, 1–5.

Baysal, E., D. D. Kosloff, and J. W. C. Sherwood, 1983, Reverse time migration: Geophysics, **48**, 1514–1524.

———, 1984, A two-way nonreflecting wave equation: Geophysics, **49**, 132–141.

Cameron, M., S. Fomel, and J. Sethian, 2008, Time-to-depth conversion and seismic velocity estimation using time-migration velocity: GEOPHYSICS, **73**, VE205–VE210.

Claerbout, J. F., 1971, Toward a unified theory of reflector mapping: Geophysics, **36**, 467–481.

———, 1985, Imaging the earth's interior: Blackwell Scientific Publications, Inc.

Díaz, E., and P. Sava, 2012, Understanding the reverse time migration backscattering: noise or signal?: SEG Technical Program Expanded Abstracts 2012, 1–6.

Etgen, J., S. Gray, and Y. Zhang, 2009, An overview of depth imaging in exploration geophysics: Geophysics, **74**, WCA5–WCA17.

Fei, T. W., Y. Luo, and G. T. Schuster, 2010, De-blending reverse-time migration: SEG Technical Program Expanded Abstracts, **29**, 3130–3134.

Fletcher, R. F., P. Fowler, P. Kitchenside, and U. Albertin, 2005, Suppressing artifacts in prestack reverse time migration: SEG Technical Program Expanded Abstracts, **24**, 2049–2051.

Fliedner, M., and D. Bevc, 2008, Automated velocity model building with wavepath tomography: Geophysics, **73**, VE195–VE204.

Gazdag, J., 1978, Wave equation migration with the phase-shift method: Geophysics, **43**, 1342–1351.

Gazdag, J., and P. Sguazzero, 1984, Migration of seismic data by phase shift plus interpolation: Geophysics, **49**, 124–131.

Gray, S., J. Etgen, J. Dellinger, and D. Whitmore, 2001, Seismic migration problems and solutions: Geophysics, **66**, 1622–1640.

Guitton, A., B. Kaelin, and B. Biondi, 2007, Least-squares attenuation of reverse-time-migration artifacts: Geophysics, **72**, S19–S23.

Kaelin, B., and C. Carvajal, 2011, Eliminating imaging artifacts in rtm using pre-stack gathers: SEG Technical Program Expanded Abstracts, **30**, 3125–3129.

Liu, F., G. Zhang, S. A. Morton, and J. P. Leveille, 2011, An effective imaging condition for reverse-time migration using wavefield decomposition: Geophysics, **76**, S29–S39.

McMechan, G. A., 1983, Migration by extrapolation of time-dependent boundary values: Geophysical Prospecting, **31**, 413–420.

Paffenholz, J., B. McLain, J. Zaske, and P. Keliher, 2002, Subsalt multiple attenuation and imaging: Observations from the sigsbee 2b synthetic dataset: 72nd Annual International Meeting, SEG, Expanded Abstracts, 2122–2125.

Plessix, R.-E., 2006, A review of the adjoint-state method for computing the gradient of a functional with geophysical applications: Geophysical Journal International, **167**, 495–503.

Pratt, R. G., 1999, Seismic waveform inversion in the frequency domain, Part I: Theory and verification in a physical scale model: Geophysics, **64**, 888–901.

Rickett, J. E., and P. C. Sava, 2002, Offset and angle-domain common image-point gathers for shot-profile migration: Geophysics, **67**, 883–889.

Sava, P., and B. Biondi, 2004, Wave-equation migration velocity analysis - I: Theory: Geophysical Prospecting, **52**, 593–606.

Sava, P., and S. Fomel, 2006, Time-shift imaging condition in seismic migration: Geophysics, **71**, S209–S217.

Sava, P., and I. Vasconcelos, 2011, Extended imaging conditions for wave-equation migration: Geophysical Prospecting, **59**, 35–55.

Sava, P., and I. Vlad, 2011, Wide-azimuth angle gathers for wave-equation migration: Geophysics, **76**, S131–S141.

Sava, P. C., and S. Fomel, 2003, Angle-domain common-image gathers by wavefield continuation methods: Geophysics, **68**, 1065–1074.

Shen, P., and W. W. Symes, 2008, Automatic velocity analysis via shot profile migration: Geophysics, **73**, VE49–VE59.

Shen, P., W. W. Symes, and C. C. Stolk, 2003, Differential semblance velocity analysis by wave-equation migration: SEG Technical Program Expanded Abstracts, **22**, 2132–2135.

Stork, C., 1992, Reflection tomography in the postmigrated domain: Geophysics, **57**, 680–692.

Symes, W., and J. Carazzone, 1991, Velocity inversion by differential semblance optimization: Geophysics, **56**, 654–663.

Symes, W. W., 2007, Reverse time migration with optimal checkpointing: Geophysics, **72**, SM213–SM221.

Tarantola, A., 1984, Inversion of seismic reflection data in the acoustic approximation: Geophysics, **49**, 1259–1266.

Weibull, W., and B. Arntsen, 2013, Automatic velocity analysis with reverse-time migration: GEOPHYSICS, **78**, S179–S192.

Whitmore, N. D., 1983, Iterative depth migration by backward time propagation: SEG Technical Program Expanded Abstracts, **2**, 382–385.

Woodward, M., 1992, Wave-equation tomography: Geophysics, **57**, 15–26.

Yang, T., and P. Sava, 2010, Moveout analysis of wave-equation extended images: Geophysics, **75**, S151–S161.

———, 2011a, Image-domain waveform tomography with two-way wave-equation: SEG Technical Program Expanded Abstracts 2011, **508**, 2591–2596.

———, 2011b, Wave-equation migration velocity analysis with time-shift imaging: Geophysical Prospecting, **59**, 635–650.

Yang, T., J. Shragge, and P. Sava, 2013, Illumination compensation for image-domain wavefield tomography: Gephysics, **78**, U65–U76.

Yoon, K., K. J. Marfurt, and W. Starr, 2004, Challenges in reversetime migration: SEG Technical Program Expanded Abstracts, 1057–1060.

Youn, O. K., and H. Zhou, 2001, Depth imaging with multiples: Geophysics, **66**, 246–255.

Zhang, Y., and J. Sum, 2009, Practical issues in reverse time migration: true amplitude gathers, noise removal and harmonic source encoding: First Break, **27**, 53–59.